A COMPUTATIONAL FRAMEWORK FOR TIME DEPENDENT DEFORMATION IN VISCOELASTIC MAGMATIC SYSTEMS

CODY RUCKER, BRITTANY A. ERICKSON, LEIF KARLSTROM, BRIAN LEE, AND JAY GOPALAKRISHNAN

Abstract. Time-dependent ground deformation is a key observable inactive magmatic systems, but is challenging to characterize. Here we present a numerical framework for modeling transient deformation and stress around a subsurface, spheroidal pressurized magma reservoir within a viscoelastic half-space with variable material coefficients, utilizing a high-order finite-element method and explicit time-stepping. We derive numerically stable time steps and verify convergence, then explore the frequency dependence of surface displacement associated with cyclic pressure applied to a spherical reservoir beneath a stress-free surface. We consider a Maxwell rheology and a steady geothermal gradient, which gives rise to spatially variable viscoelastic material properties. The temporal response of the system is quantified with a transfer function that connects peak surface deformation to reservoir pressurization in the frequency domain. The amplitude and phase of this transfer function characterize the viscoelastic response of the system,and imply a framework for characterizing general deformation timeseries through superposition. Transfer function components vary with the frequency of pressure forcing and are modulated strongly by the background temperature field. The dominantly viscous region around the reservoir is also frequency dependent, through a local Deborah number that measures pressurization period against a spatially varying Maxwell relaxation time. This near-reservoir region defines a spatially complex viscous/elastic transition whose volume depends on the frequency of forcing. Our computational and transfer function analysis framework represents a general approach for studying transient viscoelastic crustal response to magmatic forcing through spectral decomposition of deformation timeseries, such as long-duration geodetic observations.

Key points:
- A high-order numerical framework is derived for time-dependent viscoelastic deformation around magma reservoirs.
- The transfer function characterizes phase lag and amplification between pressurization at depth and surface deformation.
- The spatial extent of viscous response is frequency dependent and well-characterized by a local Deborah number.

Plain Language Summary

Ground motions associated with subsurface magma reservoirs are the result both of magma movement and time-dependent deformation of crustal rocks. We have developed a new computational framework to help interpret surface deformations associated with magmatic systems embedded within viscoelastic rocks as expected in volcanic regions. This framework is general in the sense that a broad range of scientific studies can be explored by specifying particular conditions at domain boundaries or magma reservoir geometries, and we perform rigorous numerical tests to ensure credible solutions. We then apply the model to study a simple but highly generalizable type of transient behavior - the cyclic pressurization and depressurization of a spherical reservoir. We develop a theoretical approach to simply analyze the time-dependent output, and find that temporal lag and amplification of surface deformation with respect to the reservoir pressure is explained by an aureole of material surrounding the chamber with a dominantly viscous response, whose size is frequency-dependent. Our results can be extended to many transient deformation scenarios because a sinusoidal response forms the basic element of general pressure time-series.

1. Introduction

Magma reservoirs represent a fundamental link between mantle melting and volcanic activity seen at the surface. Eruptions that drain these reservoirs are the most dramatic example of magma chamber mechanics, but a wide spectrum of time-varying surface deformation and other unrest seen in volcanic regions likely has an origin within crustal storage zones [2, 10, 32, 68]. As a result, understanding controls on time-dependent magma chamber deformation and stress is a long-standing research topic in volcanology [65, 63]. However, modeling magma reservoir evolution is a challenging problem because time-dependence may arise from a variety of physical processes occurring both internal and external to the magma transport system, many of which leave non-unique signatures in ground deformation patterns.

On sufficiently short time scales, it is appropriate to assume an elastic/brittle rheology of host rocks. Elastic models have been widely used to interpret geodetic data gathered at volcanoes [48, 46, 4]. Such models predict that time-dependent behavior comes only from reservoir magma mass balance/state variable changes [10] or boundary forcing, although poroelastic effects can also lead to time-dependence [47]. Time dependent deformation and stressing of the reservoir at longer timescales likely involves ductile response of host rocks [24, 69, 54], suggesting an overall viscoelastic rheology.

Viscoelastic effects have been identified as defining a notion of magma chamber stability, providing a mechanism for modulating stresses and deformation associated with pressurization of the chamber [15, 38, 26, 44]. Viscoelastic effects may play a role in the development of large silicic reservoirs [36] as well as eruption sequences from long-lived magma reservoirs [13] and time-dependent ground deformation at active volcanoes in diverse settings [53, 64, 45, 43, 49]. On tectonic timescales, state shifts in the magma transport system reflected by increasing intrusive-extrusive ratios, and evolving spatial organization of volcanic output around spatial centers, may also reflect time-evolving viscoelastic behavior [39].

Deformation style is strongly tied to the thermal state of the magmatic system, because both rock and magma rheology are temperature dependent. Thus it is to be expected that a viscoelastic response varies spatially, and evolves in time with the transcrustal magma transport system. Such unsteady effects, both spatial and temporal, are poorly constrained. Instead it is typically assumed that magma reservoirs reside in a steady state geotherm [14, 27, 30], or that the mechanical response is well-approximated by a pre-specified shell of viscous material in an elastic host [6, 38, 13, 62, 67]. Time evolution is often either imposed kinematically through stress boundary conditions (e.g., to model an eruptive event, [15]) or arises dynamically through mass and energy balance [38]. Viscous creep independent of time-variable forcing has also been invoked to explain deformation signals [62, 29], but general time dependent deformation has not been studied.

In this work, we address two aspects of viscoelastic deformation in magmatic systems. First, we derive and implement a high order numerical modeling framework for simulating transient thermo-mechanical behavior of a subsurface magma reservoir in an isotropic, heterogeneous, viscoelastic domain. Second, we study stress and crustal deformation associated with periodic pressure variation at the chamber wall. This represents a different sort of idealization than previous studies: we consider spatially resolved mechanical response, but treat time evolution as harmonic. In this way we isolate the frequency dependence of the viscoelastic rheology, and develop a transfer function approach using analytic functions to predict material response. This idealization might approximate some magmatic forcing scenarios, such as cyclic stress from seismic waves, periodic magma injection, or glacial cycles, and we note that quasi-periodic deformation at multiple frequencies has been observed in long-term geodetic timeseries [11].

But this approach also implies a superposition framework for studying much more general time evolution.

Our model is developed to handle general axisymmetric geometries in the subsurface and surface, including lateral loads and topographically complex material interfaces. However, we focus on the relatively simple and well-studied case of a sphere in a half-space without remote loading to explore transient effects, deriving material properties from a steady state temperature distribution within the medium. After detailing the numerical framework we verify convergence using the method of manufactured solutions [57]. Finally we use the verified framework to characterize the system's response to spatially variable viscoelastic material properties. We develop a transfer function between chamber pressure and maximum vertical surface deformation to demonstrate that two parameters – the phase lag between pressurization and surface deformation, and their relative amplitude – imply a frequency-dependent viscoelastic response that depends on chamber temperature and geothermal gradient magnitude. We demonstrate that this transfer function permits the reconstruction of complex deformation histories, and show that the spatial thermo-rheologic structure beneath the chamber influences frequency-domain expression of surface deformation.

The paper is organized with mathematical and computational details provided first, followed by the spectral (and transfer function) analysis and example calculations. In Section 2 we introduce the governing equations and generic physical problem of interest. In Section 3 we discuss the computational framework for solving our problem, stability considerations and resolution tests, and develop the specific non-dimensional time-dependent problem of interest. Readers wishing to skip such technical details can go directly to section 4, which introduces the transfer function approach that represents our primary analysis tool. Section 5 then discusses results of computations and Section 6 discusses implications for magmatic systems.

2. Mathematical Framework

2.1. **Problem Formulation and Geometry.** We consider a subsurface magma reservoir in an isotropic, viscoelastic space, see Figure 1. In general the system evolves in time in response to mass, momentum, and energy balance associated with magma transport in and out of the reservoir. We focus here on the host response to one particular state variable, a uniform but time-evolving pressure on the reservoir wall.

We employ a cylindrical coordinate system (r, z, θ) with the origin at the reservoir center. The assumption of axisymmetry means the problem shows no variation along the $\theta-$coordinate enabling solutions in the one-sided $(r, z)-$plane. Figure 1 illustrates the geometry which defines the computational region surrounding a reservoir. The magma cavity has horizontal axis $a > 0$ and vertical axis $b > 0$, with center at the origin, and Earth's free surface at $z = D + b$ (z positive upwards). Maximum depth of the computational domain is denoted by L_z and the maximum lateral distance from the center of radial symmetry is denoted by L_r.

We construct the region outside of the cavity by intersecting a closed, rectangular region $\mathcal{D} = \{(r, z) \in \mathbb{R}^2 \mid 0 < r < L_r, -L_z < z < D + b\}$ and a punctured domain $\mathcal{B} = \{(r, z) \in \mathbb{R}^2 \mid \frac{r^2}{a^2} + \frac{z^2}{b^2} > 1\}$. The region Ω outside of the cavity, defined by $\Omega = \mathcal{D} \cap \mathcal{B}$ forms our two-dimensional computational domain. The physical three-dimensional problem is posed on the revolution of Ω, the three-dimensional domain we denote by $\breve{\Omega}$.

2.2. **Governing Equations.** We assume sufficiently slow deformation so that quasi-static viscoelasticity is a valid description of the momentum balance. We assume the medium deforms according to the Maxwell constitutive law [51]. This material model is chosen for its simplicity

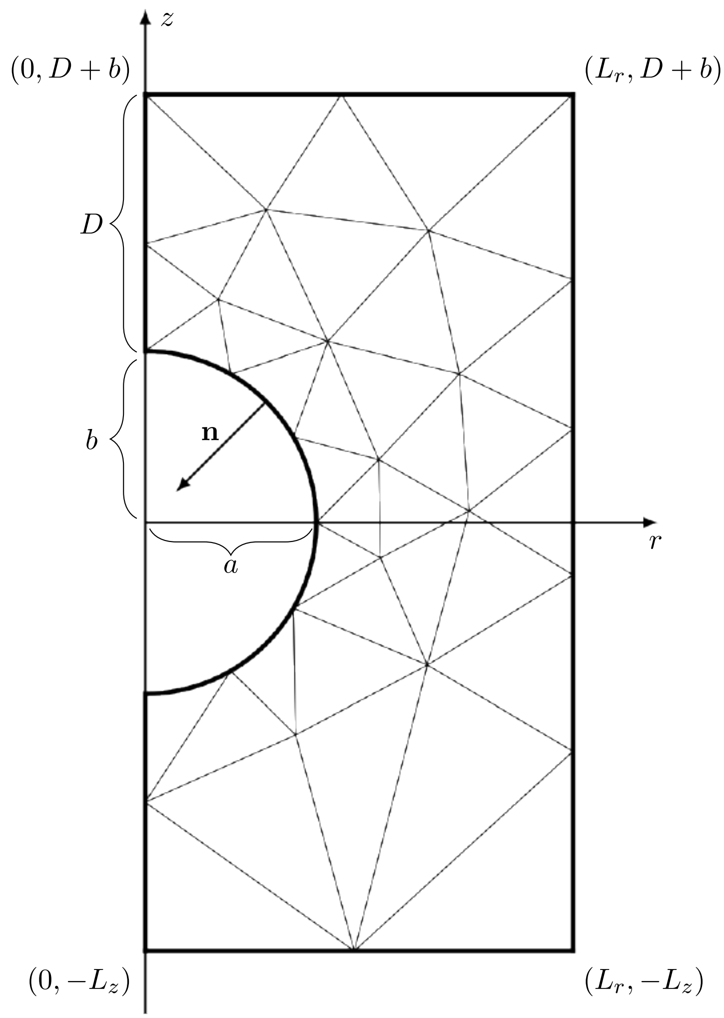

FIGURE 1. The region Ω outside a subsurface, spheroidal magma reservoir centered at the origin is discretized with a high-order FEM. The reservoir has a horizontal axis $a > 0$ and vertical axis $b > 0$. The distance from the top of the reservoir to the surface is $D > b$. The region is bounded by a maximal depth L_z and maximal distance from the radial center L_r. Though an example triangulation of the domain is shown, actual simulations are performed on a finer grid of points.

and flexibility. A variety of linear and nonlinear viscoelastic models have been proposed for crustal rocks at high temperature; the Maxwell model is a useful and easily generalizable reference case for understanding the phenomenology of viscoelastic deformation [42, 30].

Let $\mathbf{u}, \underline{\varepsilon}, \underline{\gamma}, \underline{\boldsymbol{\sigma}}$ be, respectively, the displacement vector, the total strain tensor, the viscous strain tensor, and the stress tensor. The time derivative of $\underline{\gamma}$ is denoted by $\dot{\underline{\gamma}}$. The relevant governing equations are:

$$\operatorname{div}\underline{\boldsymbol{\sigma}} = \mathbf{f} \quad \text{in } \breve{\boldsymbol{\Omega}}, \tag{1a}$$

$$\underline{\dot{\gamma}} = \boldsymbol{A}\underline{\boldsymbol{\sigma}} \quad \text{in } \breve{\Omega}, \tag{1b}$$

$$\underline{\boldsymbol{\sigma}} = \boldsymbol{E}(\underline{\boldsymbol{\varepsilon}}(\mathbf{u}) - \underline{\gamma}) \quad \text{in } \breve{\Omega}, \tag{1c}$$

where $\underline{\boldsymbol{\varepsilon}}(\mathbf{u}) = (\nabla\mathbf{u} + \nabla\mathbf{u}^T)/2$, $\boldsymbol{E}$ is the fourth-order, isotropic elastic stiffness tensor whose (i, j, k, l)-component in Cartesian coordinates is given by

$$E_{ijkl} = \lambda\delta_{ij}\delta_{kl} + \mu(\delta_{ik}\delta_{jl} + \delta_{il}\delta_{jk}). \tag{2}$$

Here, μ denotes the shear modulus, λ denotes Lamé's first parameter, and δ denotes the components of the identity tensor. The fourth-order tensor $\boldsymbol{A}$ relates viscous strain to stress, and is derived from the Maxwell constitutive law [51] to produce the form

$$\boldsymbol{A}\underline{\boldsymbol{\sigma}} = \frac{1}{2\eta}\left(\sigma_{ij} - \frac{1}{3}\sigma_{kk}\delta_{ij}\right), \tag{3}$$

where η denotes the viscosity and repeated indices indicate summation over that index.

Equation (1a) is the static equilibrium equation where $\mathbf{f}$ represents body forces. Equation (1b) is the aging law for a Maxwell material and Equation (1c) is Hooke's Law. When supplemented by initial and boundary conditions, the system (1a) can be solved in any coordinate system.

We use the cylindrical coordinate system (r, z, θ), writing the displacement vector field as $\mathbf{u} = u_r\boldsymbol{e}_r + u_z\boldsymbol{e}_z + u_\theta\boldsymbol{e}_\theta$ where $\boldsymbol{e}_r, \boldsymbol{e}_\theta$, and $\boldsymbol{e}_z$ denote the unit vectors of the cylindrical coordinate system. The source $\mathbf{f}$ can also be similarly expressed. We assume that u_θ and f_θ are zero. Furthermore, by the assumption of axial symmetry, u_r and u_z are independent of θ. Hence, employing the cylindrical components of the strain tensor, displacements in the Earth are related to strains by

$$\underline{\boldsymbol{\varepsilon}}(\mathbf{u}) = \frac{u_r}{r}\boldsymbol{e}_\theta \otimes \boldsymbol{e}_\theta + \sum_{i,j\in\{r,z\}} \frac{1}{2}(\partial_i u_j + \partial_j u_i)\boldsymbol{e}_i \otimes \boldsymbol{e}_j. \tag{4}$$

The stress tensor can be expressed, omitting its zero components, as

$$\underline{\boldsymbol{\sigma}} = \sigma_{\theta\theta}\boldsymbol{e}_\theta \otimes \boldsymbol{e}_\theta + \sum_{i,j\in\{r,z\}} \sigma_{ij}\boldsymbol{e}_i \otimes \boldsymbol{e}_j. \tag{5}$$

The equilibrium equation (1a) then takes the form

$$\left(\partial_r\sigma_{rr} + \partial_z\sigma_{rz} + \frac{1}{r}(\sigma_{rr} - \sigma_{\theta\theta})\right)\boldsymbol{e}_r + \left(\partial_r\sigma_{rz} + \partial_z\sigma_{zz} + \frac{1}{r}\sigma_{rz}\right)\boldsymbol{e}_z = \mathbf{f}. \tag{6}$$

Using (4) and (1c) to obtain expressions for the cylindrical components of the stress tensor, the equilibrium equation (6) can be solved for the components of the displacement in the two-dimensional meridian (rz) plane.

To reduce the problem to the meridian half-plane where $r > 0$, we need to impose the following boundary conditions on the axial boundary $\Gamma_0 = \{(r, z) \in \partial\Omega : r = 0\}$, namely

$$u_r = 0, \quad \text{on } \Gamma_0 \tag{7a}$$

$$\sigma_{rz} = 0, \quad \text{on } \Gamma_0. \tag{7b}$$

The first follows from a "no-opening" condition at $r = 0$. The second comes from requiring continuity of stresses in the $\boldsymbol{e}_z$ direction at $r = 0$. Other boundary conditions are imposed by partitioning the remaining boundary $\partial\Omega \setminus \Gamma_0$. We let $\Gamma_{\text{disp}} \subseteq \partial\Omega$ and $\Gamma_{\text{trac}} = \partial\Omega \setminus \Gamma_{\text{disp}}$ denote a general partitioning of $\partial\Omega$ into subdomains where either displacement or traction boundary conditions are imposed, respectively. Explicitly, these conditions are

$$\mathbf{u} = \mathbf{g}_{\text{disp}}(t) \quad \text{on } \Gamma_{\text{disp}}, \tag{7c}$$

$$\underline{\boldsymbol{\sigma}} \cdot \mathbf{n} = \mathbf{g}_{\text{trac}}(t) \quad \text{on } \Gamma_{\text{trac}}, \tag{7d}$$

where $\mathbf{n}$ is the outward unit normal to the domain Ω, and $\mathbf{g}_{\text{disp}}$, $\mathbf{g}_{\text{trac}}(t)$ are given, time-varying boundary data. This general model enables the study of reservoir pressure, lateral loads and topography, among other studies in axisymmetric geometries.

In addition to boundary conditions, we must also supplement the aging law, Equation (1b), with an initial condition on viscous strain, namely

$$\underline{\boldsymbol{\gamma}}(r, z, t = 0) = \underline{\boldsymbol{\gamma}}_0(r, z), \qquad (r, z) \in \Omega. \tag{8}$$

3. Computational Framework

We solve initial-boundary-value problem (Equations (1a),(4)-(8)) numerically by pairing a finite difference discretization in time with a high-order finite element method (FEM) in space. As described in this section, at each time step the spatial problem is governed by static equilibrium, with viscous effects manifested as a time-dependent source term. Simulations are done using Python code developed on top of the free and open source multi-physics library NGSolve [60] and the accompanying mesh generator [59]. The Python code is available in a public repository [23]. We use a two-dimensional mesh of triangles. To capture the magma chamber boundary accurately, we use nonlinear mappings for those elements with edges on the curved boundary to improve geometrical conformity [19]. The following subsections outline the static problem, the temporal discretization, and the details of the specific problem considered in this work.

3.1. Solving the Static Equilibrium Equation.

We solve the equilibrium equations (1a) subject to boundary conditions (7) using a FEM, which requires the weak form of the problem. To construct the weak form, we perform the following steps: (i) multiply equation (6) by r and take the dot product of both sides with a test function $\mathbf{v} = v_r \boldsymbol{e}_r + v_z \boldsymbol{e}_z$, (ii) integrate by parts on Ω, (iii) replace σ_{ij} by functions of u_i using (4) and (1c), and (iv) incorporate the boundary conditions of (7), letting $\mathbf{v}$ take on homogeneous displacement boundary conditions on Γ_{disp}. The result is the equation

$$\int_\Omega \boldsymbol{E}(\underline{\boldsymbol{\varepsilon}}(\mathbf{u}) - \underline{\boldsymbol{\gamma}}) : \underline{\boldsymbol{\varepsilon}}(\mathbf{v})\, r\, dr dz - \int_{\Gamma_{\text{trac}}} \mathbf{g}_{\text{trac}} \cdot \mathbf{v}\, r\, ds = -\int_\Omega \mathbf{f} \cdot \mathbf{v}\, r\, dr dz. \tag{9}$$

Here the colon denotes the Frobenius inner product. To simplify notation, we let $(\cdot, \cdot)_r$ and $\langle \cdot, \cdot \rangle_r$ respectively denote the integrals over Ω and Γ_{trac} of r multiplied by the appropriate (dot or Frobenius) inner product of the arguments. Then the above equation may be rewritten as

$$(\boldsymbol{E}\underline{\boldsymbol{\varepsilon}}(\mathbf{u}), \underline{\boldsymbol{\varepsilon}}(\mathbf{v}))_r = -(\mathbf{f}, \mathbf{v})_r + \langle \mathbf{g}_{\text{trac}}, \mathbf{v} \rangle_r + (\boldsymbol{E}\boldsymbol{\gamma}, \mathbf{v})_r. \tag{10}$$

The Lagrange FEM is derived by imposing the above equation on a space of piecewise polynomials. Given a triangulation of Ω, denoted by Ω_h, the Lagrange finite element space of order p, denoted by V_h consists of all functions which are continuous on Ω whose restriction to each element K of Ω_h is a polynomial of degree at most p in r and z. The method is high-order, meaning that polynomials of high degree within each mesh element approximate the solution. When degree p is used within an element of diameter h, the solution can be approximated on that element at rate $O(h^{p+1})$. As h decreases, the solution becomes smoother, thus using higher p means that the numerical solution is more rapidly convergent than a low-order method. In the FEM, the data $\mathbf{f}$ and $\mathbf{g}_{\text{trac}}$ are integrated while the data $\mathbf{g}_{\text{disp}}$ is interpolated. Assuming the latter interpolation is done, let

$$\boldsymbol{V}_h^{\mathbf{g}_{\text{disp}}} = \{\mathbf{v} = v_r\boldsymbol{e}_r + v_z\boldsymbol{e}_z : v_r \in V_h, v_z \in V_h, \text{ and } \mathbf{v}|_{\Gamma_{\text{disp}}} = \mathbf{g}_{\text{disp}}\}.$$

Also let

$$\boldsymbol{V}_h^0 = \{\mathbf{v} = v_r\boldsymbol{e}_r + v_z\boldsymbol{e}_z : v_r \in V_h, v_z \in V_h, \text{ and } \mathbf{v}|_{\Gamma_{\text{disp}}} = \mathbf{0}\}.$$

Then, the FEM computes $\mathbf{u}_h \in \boldsymbol{V}_h^{\mathbf{g}_{\text{disp}}}$ satisfying

$$(\boldsymbol{E}\underline{\boldsymbol{\varepsilon}}(\mathbf{u}_h), \underline{\boldsymbol{\varepsilon}}(\mathbf{v}))_r = -(\mathbf{f}, \mathbf{v})_r + \langle \mathbf{g}_{\text{trac}}, \mathbf{v}\rangle_r + (\boldsymbol{E}\boldsymbol{\gamma}, \mathbf{v})_r, \qquad \text{for all } \mathbf{v} \in \boldsymbol{V}_h^0, \tag{11}$$

provided $\mathbf{f}, \mathbf{g}_{\text{disp}}, \mathbf{g}_{\text{trac}}$, and $\boldsymbol{\gamma}$ are given. Equation (11) leads to a linear system of equations once a finite element basis of shape functions (which are basis functions determining one degree of freedom in the finite element system) is used.

3.2. **Temporal Discretization.** Our time-stepping method is inspired by that of [1] where viscous strains appear as a time-dependent source term on the equilibrium equation: As can be seen from Equation (11), once $\boldsymbol{\gamma}$ is known at any given time, it appears as a known term and a displacement approximation can be computed by solving (11). However, to compute $\boldsymbol{\gamma}$, we need to apply a time integrator to the aging law, Equation (1b).

To this end, for computational purposes only it is convenient to let $\underline{\boldsymbol{C}} = \boldsymbol{E}\underline{\boldsymbol{\gamma}}$, since the use of $\underline{\boldsymbol{C}}$ allows us to skip the assembly and inversion of a mass matrix made of inhomogeneous material coefficients. Since $\boldsymbol{E}$ is time independent, simplifying $\boldsymbol{E}\boldsymbol{A}\underline{\boldsymbol{\sigma}} = (\mu/\eta)\text{dev}(\underline{\boldsymbol{\sigma}})$, Equation (1b) implies

$$\dot{\underline{\boldsymbol{C}}} = \frac{\mu}{\eta}\,\text{dev}\,\underline{\boldsymbol{\sigma}}. \tag{12}$$

Here $\text{dev}(\underline{\boldsymbol{\sigma}})$ denotes deviatoric tensor $\underline{\boldsymbol{\sigma}} - \text{tr}(\underline{\boldsymbol{\sigma}})$. Time integration of Equation (12) is carried out using the first-order accurate forward Euler method (chosen for its simplicity as we lay the computational groundwork; higher order methods will be incorporated in future developments). At each time step, we solve the weak form of equilibrium equation (Equation (11)) and use the computed displacement to obtain $\underline{\boldsymbol{C}}$ at the next time step. To illustrate time-stepping explicitly, assume all fields are known at time t^n. The procedure to integrate to t^{n+1} over step size $\Delta t = t^{n+1} - t^n$ is as follows:

(1) Use $\mathbf{u}_h^n$ to update $\underline{\boldsymbol{C}}$ via forward Euler

$$\underline{\boldsymbol{C}}^{n+1} = \underline{\boldsymbol{C}}^n + \Delta t\frac{\mu}{\eta}\,\text{dev}\left(\boldsymbol{E}\underline{\boldsymbol{\varepsilon}}(\mathbf{u}_h^n) - \underline{\boldsymbol{C}}^n\right). \tag{13}$$

(2) Compute data $\mathbf{f}^{n+1}$, $\mathbf{g}_{\text{disp}}^{n+1}$, $\mathbf{g}_{\text{trac}}^{n+1}$ at time t^{n+1} and use them, together with the output of the previous step, to solve the static equation: compute $\mathbf{u}_h^{n+1} \in \boldsymbol{V}_h^{\mathbf{g}_{\text{disp}}^{n+1}}$ satisfying

$$(\boldsymbol{E}\underline{\boldsymbol{\varepsilon}}(\mathbf{u}_n^{n+1}), \underline{\boldsymbol{\varepsilon}}(\mathbf{v}))_r = -(\mathbf{f}^{n+1}, \mathbf{v})_r + \langle \mathbf{g}_{\text{trac}}^{n+1}, \mathbf{v}\rangle_r + (\underline{\boldsymbol{C}}^{n+1}, \mathbf{v})_r \tag{14}$$

for all $\mathbf{v} \in \boldsymbol{V}_h^0$.

Verification of both spatial and temporal convergence of this computational method follows in section 3.4.

3.3. Model Specifics and Non-Dimensionalization. The majority of analysis in this work will examine how a spatial distribution of viscoelastic properties impacts deformation around magma reservoirs subject to cyclic loading. We proceed by idealizing the boundary pressure as a sinusoid, which approximates a canonical problem in viscoelasticity [20,], and provides a framework for studying arbitrary time dependent signals through superposition. We thus assume a specific boundary partition where Γ_{trac} encompasses the reservoir wall, Earth's free surface, and the computational boundary at depth ($z = -L_z$). Γ_{disp} is the lateral boundary $r = L_r$. We then set specific boundary data

$$\mathbf{g}_{\text{disp}}(t) = 0, \tag{15}$$

so that displacements vanish at $r = L_r$. At Earth's free surface and at depth we take

$$\mathbf{g}_{\text{trac}}(t) = 0. \tag{16}$$

At the reservoir wall we set

$$-\mathbf{n} \cdot \mathbf{g}_{\text{trac}}(t) \quad = P(t), \tag{17a}$$

$$\mathbf{m} \cdot \mathbf{g}_{\text{trac}}(t) \quad = 0, \tag{17b}$$

where

$$P(t) = P_0 \sin(\omega t). \tag{18}$$

Equation 17a sets the normal component of the traction vector (the pressure) equal to a sinusoidal time-varying condition with amplitude P_0 and frequency ω. In what follows we will often refer to forcing period

$$\tau = 2\pi/\omega \tag{19}$$

rather than frequency. Equation 17b imposes that the shear component of traction be equal to 0, where vector $\mathbf{m} = \mathbf{n} \times \boldsymbol{e}_{\mathbf{z}}$ is tangent to the reservoir wall.

Non-dimensionalization of the governing equations reveals important physical parameters and re-scales the problem to help reduce round-off errors. We begin by handling the scaling of the spatial domain before addressing governing equations. Tildes in what follows indicate non-dimensional variables. Let $r = a\tilde{r}$, $z = a\tilde{z}$, $\widetilde{\mathcal{D}} = \{(\tilde{r}, \tilde{z}) \in \mathbb{R}^2 \mid 0 \leq \tilde{r} \leq \frac{L_r}{a}, -\frac{L_z}{a} \leq \tilde{z} \leq \frac{D+b}{a}\}$ and $\tilde{\mathcal{B}} = \{(\tilde{r}, \tilde{z}) \in \mathbb{R}^2 \mid \tilde{r}^2 + \frac{a^2}{b^2}\tilde{z} \geq 1\}$. Then our resulting scaled domain is given by

$$\tilde{\Omega} = \widetilde{\mathcal{D}} \cap \tilde{\mathcal{B}}, \tag{20}$$

with scaled boundaries $\tilde{\Gamma}_{\text{disp}}$ still representing the (scaled) lateral boundary and $\tilde{\Gamma}_{\text{trac}}$ the (scaled) reservoir wall, Earth's free surface, and computational boundary at depth. We also scale displacements by a, namely $a\tilde{\underline{\boldsymbol{u}}} = \underline{\boldsymbol{u}}$, which effectively means that total strain $\underline{\boldsymbol{\epsilon}}$ is not scaled. We scale stress and time by the amplitude and frequency of the sinusoidal pressure, $\boldsymbol{E}$ by characteristic shear modulus μ and body force by its magnitude F_0 (for example magnitude of gravitational force), giving

$$\underline{\boldsymbol{\sigma}} \quad = \quad P_0 \tilde{\underline{\boldsymbol{\sigma}}}, \tag{21}$$

$$\boldsymbol{E} \quad = \quad \mu \widetilde{\boldsymbol{E}}, \tag{22}$$

$$\mathbf{f} \quad = \quad F_0 \widetilde{\mathbf{f}}, \tag{23}$$

$$t\omega \quad = \quad \tilde{t}, \tag{24}$$

which implies a scaling of $\underline{\boldsymbol{C}} = P_0 \widetilde{\underline{\boldsymbol{C}}}$. The scaled form of the equilibrium equation (1a) is thus

$$\operatorname{div} \tilde{\underline{\boldsymbol{\sigma}}} = \frac{aF_0}{P_0} \widetilde{\mathbf{f}}, \tag{25}$$

and Hooke's law Equation (1c) becomes

$$\tilde{\underline{\boldsymbol{\sigma}}} = \frac{\mu}{P_0}\widetilde{\boldsymbol{E}}(\underline{\boldsymbol{\varepsilon}} - \underline{\boldsymbol{\gamma}}). \tag{26}$$

The two dimensionless parameters in Equations 25-26 physically represent the ratio of body force to reservoir boundary tractions, and a scaled reservoir pressure, respectively.

The modified aging law (Equation (12)) becomes

$$\partial_{\tilde{t}}\underline{\widetilde{\boldsymbol{C}}} = \frac{1}{De}\operatorname{dev}\tilde{\sigma}, \tag{27}$$

where

$$De = \frac{\eta\omega}{\mu} = \frac{2\pi\eta}{\tau\mu} \tag{28}$$

is the non-dimensional Deborah number, a ratio of elastic pressurization timescale $\tau/2\pi$ to Maxwell viscous relaxation timescale η/μ, where viscosity η, shear modulus μ and pressurization time τ are understood to be characteristic scales if spatially or time variable. De commonly appears as a control parameter in models for magma chamber mechanics [36, 34,], cycles of eruptions [13, 5,], and the spatial structure of transcrustal magma systems [39, 35,]. It will play an important role in our results.

Computationally, all problems considered in this work are solved in this non-dimensional form. The specific non-dimensional boundary conditions we thus take are

$$\tilde{\underline{\boldsymbol{u}}} = 0 \qquad \text{on } \tilde{\Gamma}_{\text{disp}}, \tag{29a}$$

$$\tilde{\underline{\boldsymbol{\sigma}}}\mathbf{n} = \tilde{\mathbf{g}}_{\text{trac}}(\tilde{t}) \qquad \text{on } \tilde{\Gamma}_{\text{trac}}, \tag{29b}$$

and at the reservoir wall,

$$-\mathbf{n}\cdot\tilde{\mathbf{g}}_{\text{disp}}(\tilde{t}) = \tilde{P}(\tilde{t}) \tag{30}$$

$$\mathbf{m}\cdot\tilde{\mathbf{g}}_{\text{trac}}(\tilde{t}) = 0. \tag{31}$$

where $\tilde{P}(\tilde{t}) = \sin(\tilde{t})$. For all our applications we assume negligible body forces, so $aF_0/P_0 \ll 1$.

3.4. **Stability and Verification.** Owing to the use of an explicit time-stepping scheme, it is necessary to establish conditions for which the scheme outlined in the previous section is stable. As an initial calculation, note that

$$\boldsymbol{E}\boldsymbol{A}\underline{\boldsymbol{\sigma}} = \frac{\mu}{\eta}\operatorname{dev}\underline{\boldsymbol{\sigma}}. \tag{32}$$

The deviatoric operator in Equation (32) can be expressed as a matrix-vector multiplication, namely

$$\boldsymbol{E}\boldsymbol{A}\underline{\boldsymbol{\sigma}} = \frac{\mu}{\eta}\mathscr{D}\underline{\boldsymbol{\sigma}}, \tag{33}$$

if second-order tensors are stacked into vectors (across rows and removing symmetries)

$$\underline{\boldsymbol{\sigma}} = \left[\sigma_{rr},\ \sigma_{rz},\ \sigma_{zz},\ \sigma_{\theta\theta}\right]^T, \tag{34}$$

and matrix $\mathscr{D}$ is given by

$$\mathscr{D} = \begin{bmatrix} \frac{2}{3} & -\frac{1}{3} & -\frac{1}{3} & 0 \\ -\frac{1}{3} & \frac{2}{3} & -\frac{1}{3} & 0 \\ -\frac{1}{3} & -\frac{1}{3} & \frac{2}{3} & 0 \\ 0 & 0 & 0 & 1 \end{bmatrix}. \tag{35}$$

The non-dimensionalized explicit forward-Euler discretization of the aging law (Equation (27)) can therefore be expressed as

$$\underline{\widetilde{\boldsymbol{C}}}^{n+1} = (\boldsymbol{I} - \Delta\tilde{t}De^{-1}\mathscr{D})\underline{\widetilde{\boldsymbol{C}}}^{n} + \Delta\tilde{t}De^{-1}\mathscr{D}\widetilde{\boldsymbol{E}}\underline{\boldsymbol{\varepsilon}}^{n}, \tag{36}$$

the stability of which is determined by the eigenvalues of the growth-factor matrix $\boldsymbol{I} - \Delta tDe^{-1}\mathscr{D}$ and whether we can bound its spectral radius using an appropriate choice for Δt. Eigenvalues for the growth-factor matrix are

$$\lambda_1 = 1, \tag{37a}$$

$$\lambda_2 = 1 - \frac{2}{3}\Delta\tilde{t}De^{-1}, \tag{37b}$$

$$\lambda_3 = 1 - \Delta\tilde{t}De^{-1}, \tag{37c}$$

where λ_3 appears as a repeated eigenvalue. To bound their magnitudes by at most 1 demands that $\Delta\tilde{t}$ be smaller than $2De$. In addition, the time step must be sufficiently small to resolve any time-varying boundary data. In this work this amounts to resolving the sinusoidal boundary data at the reservoir wall. Since the corresponding (angular) Nyquist frequency for $\sin(\tilde{t})$ is 1, the largest time step that resolves this frequency is $\delta\tilde{t} = \pi$, and should be (in practice) a small fraction of this. A sufficient, stable time step is then chosen by

$$\Delta\tilde{t} \leq \min\{2De, \delta\tilde{t}\}. \tag{38}$$

In practice we use more restrictive criteria, namely,

$$\Delta\tilde{t} \leq \min\left\{\frac{De}{4}, \frac{\delta\tilde{t}}{2}\right\}. \tag{39}$$

Except for a few limiting cases, the temperature-dependent material parameters will cause $\frac{De}{4}$ to be the agent that restricts time-step.

Our numerical method is verified for correctness via rigorous convergence tests in both space and time via the method of manufactured solutions (MMS) [57], with details provided in A. Code verification could also be done via comparisons against simple analytic models [33], or benefit from community benchmark efforts, which we further discuss in A.

3.5. **Temperature-Dependent Material Parameters.** We assume that viscosity of crustal rocks is described by a temperature-dependent Arrhenius relation, an assumption common to many thermomechanical models of magmatic systems [14]. This neglects grain-size and stress-dependent effects [7,], but parameterizes our assumption that temperature is the dominant factor controlling crustal rheology during crustal magma transport. In general, temperature evolves in time in response to magmatism [37], but we assume a steady state geotherm here as our goal is simply to explore the role of realistic spatial structure of material parameters.

Accordingly, we solve the stationary heat equation

$$\nabla^2 T = 0 \qquad \text{in } \breve{\Omega}, \tag{40}$$

where $T(r,z)$ is the temperature field, which we assume to be axisymmetric. At the top, bottom and lateral parts of the boundary, we enforce a steady-state geothermal profile given by

$$T(z) = T_s - \alpha\big(z - (D+b)\big), \tag{41}$$

where T_s is the surface temperature constant and α is a parameter specifying the temperature gradient. At the chamber wall we set $T = T_c$, a constant temperature. We use a finite element space of order p to solve the heat equation. Here, p is the same order as is used in the finite element solution of the equilibrium equation. The formulation uses radial weighting to reduce the problem to the two-dimensional domain Ω and as usual–see e.g., [22]—set zero temperature flux $\nabla T = 0$ at Γ_0, the $r = 0$ boundary, to maintain our consideration of a one-sided problem. The solution of this BVP for the heat equation informs the temperature field throughout the domain, from which the viscosity is deduced according to the Arrhenius formula

$$\eta = A_D \exp\left(\frac{E_a}{RT}\right) \tag{42}$$

where A_D is the Dorn parameter, E_a is the activation energy, and R is the Boltzmann constant. For numerical computation, we prefer to use the equivalent formula

$$\eta = \eta_0 \exp\left(\frac{E_a}{R}\left[\frac{1}{T} - \frac{1}{T_s}\right]\right), \tag{43}$$

where $\eta_0 = A_D \exp\left(\frac{E_a}{RT_s}\right)$, to avoid numerical issues associated with very large viscosities predicted by low temperatures in the near surface. In Equation 43 we use absolute temperature, so both T and T_s should be converted from degrees Celsius to Kelvin.

Because numerically stable time steps depend on Deborah number (i.e. Equation 38) in our approach, the exponential dependence of viscosity leads to prohibitively small time steps at high temperatures. This limits the degree to which we can exactly explore high magma temperatures without artificially thresholding model temperature.

Elastic parameters are also considered to be temperature dependent. [3] provide smooth and continuous forms for temperature-dependent Young's modulus $E(T)$ and Poisson's ratio $\nu(T)$ as

$$E(T) = c_1\left[1 - \operatorname{erf}\left(\frac{T - \bar{T}}{s}\right)\right] + c_2 T + c_3, \tag{44}$$

$$\nu(T) = \left[1 - \frac{E}{E_{\max}}\right] \cdot [\nu_{\max} - \nu_{\min}] + \nu_{\min} \tag{45}$$

where $\nu_{\min} = 0.25, \nu_{\max} = 0.49$ define the range of possible Poisson's ratios and $E_{\max}$ is the max value Young's modulus achieves for a given temperature profile. $\bar{T}$ is a temperature threshold for which Young's modulus decreases by an order of magnitude and c_1, c_2, c_3, s are empirical parameters. To convert E and ν to λ, μ (the proper elastic moduli for our framework), we use $\lambda = \frac{E\nu}{(1+\nu)(1-2\nu)}$, $\mu = \frac{E}{2(1+\nu)}$. Figure 3 demonstrates the spatial pattern exhibited by the material parameters for a temperature profile characterized by 800°C reservoir temperature, 0°C surface temperature and a geothermal gradient of 20°C/km.

4. Analysis of time dependent viscoelastic deformation

We now develop tools to analyze the time evolution of viscoelastic deformation predicted from our numerical calculations. Towards our goal of examining how a realistic distribution of

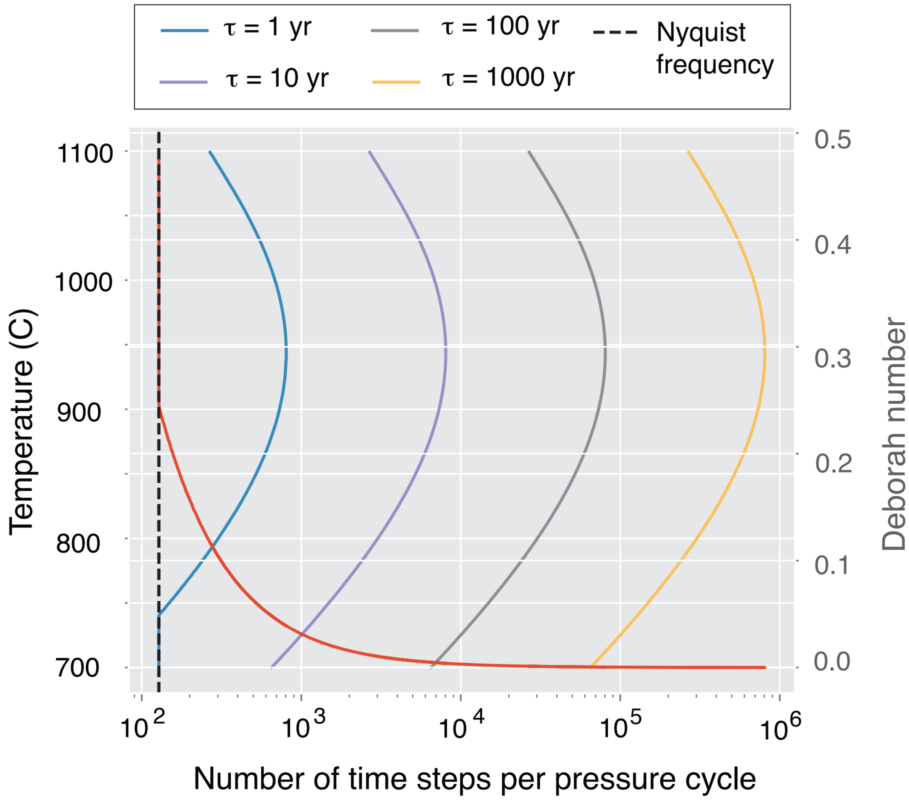

FIGURE 2. Number of timesteps required to simulate pressure forcing of various periods. Number of timesteps decreases with increasing Deborah number (red curve), until the Nyquist limit is reached (dashed curve). Number of timesteps per period is a non-monotonic function of temperature (other colored curves) because both elastic moduli and viscosity are temperature dependent.

viscoelastic properties impacts deformation around magma reservoirs subject to cyclic loading, we begin with a 1D analysis of the Maxwell model to illustrate inherent properties of the system which may be generalized in the 2D problem. This analysis is easily generalizable to other viscoelastic models, and leads to concrete implications for inferring viscoelastic behavior in magmatic systems from ground deformation.

4.1. **Insights from the 1D Maxwell Model.** Given the spatial domain $x \in [0, L]$, the 1D strain-displacement relation is given by

$$\varepsilon = u_x \tag{46}$$

and the 1D governing equations (equilibrium, viscous strain evolution and Hooke's law, respectively) are

$$\frac{\partial \sigma}{\partial x} = 0, \tag{47a}$$

$$\dot{\gamma} = \frac{1}{\eta}\sigma, \tag{47b}$$

$$\sigma = \mu(\varepsilon - \gamma), \tag{47c}$$

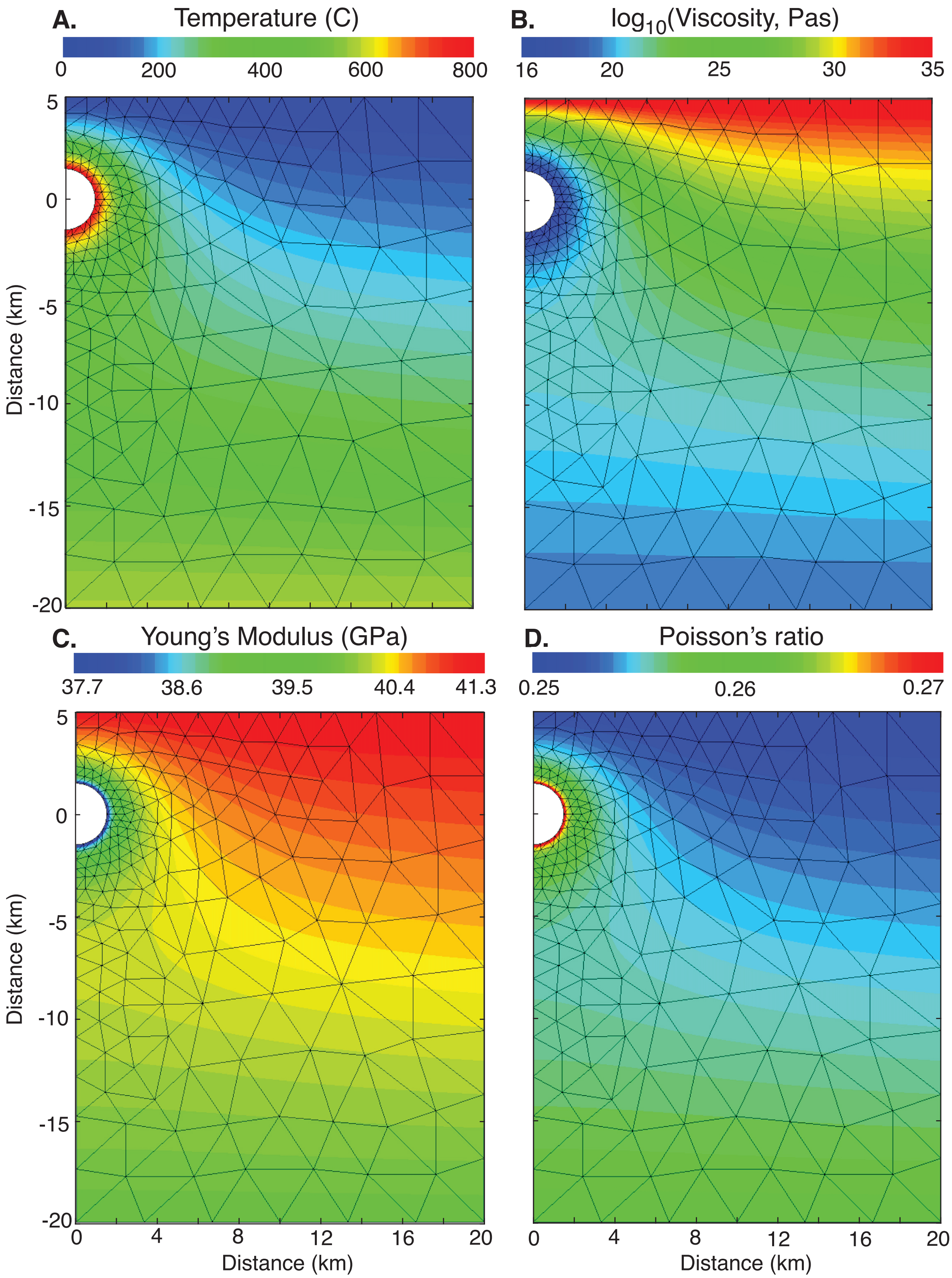

FIGURE 3. Material parameters used in our reference variable coefficients parameter study, with finite element mesh overlaid. **A.** Temperature, obtained by solving Equation 40 with $T_c = 800°\text{C}$, surface temperature $T_s = 0°\text{C}$, and geothermal gradient $\alpha = 20°\text{C/km}$. **B.** Viscosity from Equation 43. **C.** Young's Modulus from Equation 44. **D.** Poisson's ratio from Equation 45.

where σ, ε, γ, and u are, respectively, the 1D stress, total strain, viscous strain, and displacement. Boundary conditions are chosen to reflect the conditions for the 2D problem. The origin experiences the sinusoidal pressure condition (representing the reservoir) and displacements vanish at the far boundary, namely

$$\sigma\big(x=0,t\big) = \sin(\omega t), \tag{48a}$$

$$u\big(x=L,t\big) = 0. \tag{48b}$$

We consider $t > 0$; the aging law Equation 47b thus requires an initial viscous strain to be specified, which we express in general terms

$$\gamma\big(x,t=0\big) = \gamma_0(x), \tag{49}$$

where γ_0 as a given function. The Maxwell model thus gives rise to an initial-boundary value problem defined by Equations 46-49.

We are interested in the response between stress and strain at the reservoir boundary, with the expectation that viscous relaxation will lead to a phase difference. To do this analysis it is useful to work with Hooke's law in rate form, namely,

$$\dot{\varepsilon} = \frac{1}{\mu}\dot{\sigma} + \frac{1}{\eta}\sigma. \tag{50}$$

Following [20], application of the Fourier transform to Equation 50 yields the constitutive law in frequency space

$$\hat{\sigma}(\omega) = \hat{\mu}(\omega)\hat{\varepsilon}(\omega), \tag{51}$$

which gives the usual relationship where stress is expressed as a function of strain through a complex shear modulus $\hat{\mu}$ defined by

$$\hat{\mu}(\omega) = \left(\frac{1}{\mu} - i\frac{1}{\eta\omega}\right)^{-1}. \tag{52}$$

The decomposition $\hat{\mu}(\omega) = \hat{\mu}_1(\omega) + i\hat{\mu}_2(\omega)$ into storage and loss moduli allows us to express $\hat{\mu}$ as

$$\hat{\mu}(\omega) = |\hat{\mu}(\omega)|e^{-i\delta} \tag{53}$$

where $\delta = -\tan^{-1}(\frac{\hat{\mu}_2}{\hat{\mu}_1})$.

In our applications, however, we are interested in the strain response to an applied (sinusoidal) stress, thus we must consider the constitutive relation Equation 51 in the form

$$\hat{\varepsilon}(\omega) = \hat{d}(\omega)\hat{\sigma}(\omega), \tag{54}$$

where $\hat{d}(\omega) = 1/\hat{\mu}(\omega)$ is the complex creep modulus given by

$$\hat{d}(\omega) = \frac{1}{\mu} - i\frac{1}{\eta\omega}, \tag{55}$$

which can be decomposed into $\hat{d}(\omega) = \hat{d}_1(\omega) + i\hat{d}_2(\omega)$ as before, and gives rise to the similar form

$$\hat{d}(\omega) = |\hat{d}(\omega)|e^{-i\beta}, \tag{56}$$

for $\beta = -\tan^{-1}\left(\frac{\hat{d}_2(\omega)}{\hat{d}_1(\omega)}\right)$. Applying the inverse Fourier transform to Equation 54 and using 48a yields

$$\begin{aligned}\varepsilon(t) &= [d * \sigma](t), \\ &= \hat{d}_1(\omega)\sin\omega t + \hat{d}_2(\omega)\cos\omega t, \\ &= \sin(\omega t - \beta),\end{aligned} \tag{57}$$

which gives strain as an explicit function of stress, delayed by phase lag β. Since $\hat{d}$ is chosen as the multiplicative inverse of $\hat{\mu}$ note that

$$|\hat{d}(\omega)| = \frac{1}{|\hat{\mu}(\omega)|}, \tag{58a}$$

$$\beta = -\delta, \tag{58b}$$

therefore the phase lag that strain experiences in response to an applied stress will be equal and opposite when reversing roles and considering stress in response to an applied strain. Note that we have used the sign convention for the phase lag such that positive values of β correspond to strain lagging behind stress.

To summarize, the strain response to a sinusoidal stress is also sinusoidal with a phase lag β, which can be simplified in terms of the Deborah number De by substituting in the real and imaginary parts of $\hat{d}(\omega)$, resulting in

$$\beta = \tan^{-1}\left(\frac{1}{De}\right). \tag{59}$$

This analytic result provides insight into the physics of the viscoelastic model, as two limiting cases of the Deborah number (namely $De \to \infty$ and $De \to 0$) yield phase lags of 0 and $\pi/2$ (respectively) corresponding to the elastic and viscous limits (respectively). In addition, these analytic results can be generalized to higher dimensions which we do in the next section, providing useful code verification metrics as well as providing insight into the frequency response of more physically realistic modeling scenarios.

4.2. **Transfer Function and Analytic Signals.** The phase lag analysis for the 1D problem of the previous section can be generalized using the theory of Linear Time-Invariant (LTI) systems such as the viscoelastic problem we consider here. For general LTI systems, one can characterize some output signal $y(t)$ as the linear transformation of a system input $x(t)$, where we consider one-sided signals (i.e. they are 0 for $t < 0$) [58]. The response y can be determined as a convolution of the input x with the system impulse response h, namely

$$\begin{aligned}y(t) &= (x * h)(t) \\ &= \int_0^t x(t')h(t-t')\,dt'.\end{aligned} \tag{60}$$

The transfer function connecting the output signal $y(t)$ given the input signal $x(t)$ we denote $H\{y(t)\,|\,x(t)\}(i\omega)$, however we drop the argument within curly braces or functional dependence within parenthesis when these is implied via context. The transfer function is defined as

$$\begin{aligned}H(i\omega) &= \mathcal{L}\{h\}(i\omega) \\ &= \frac{\mathcal{L}\{y\}}{\mathcal{L}\{x\}}(i\omega),\end{aligned} \tag{61}$$

where $\mathcal{L}$ denotes the Laplace transform (a function of the complex variable s) and we have evaluated at $s = i\omega$. The transfer function thus provides the amplitude of the system output as a function of frequency of the input signal. As an example, Equation 54 illustrates how $\hat{d} = H\{\varepsilon(t) \,|\, \sigma(t)\}$, i.e the transfer function when stress is the input signal and strain is the output.

If we consider specific input and output signals $x(t) = A_{in} \sin(\omega t)$ and $y(t) = A_{out} \sin(\omega t - \phi)$, then we can use the Laplace transform to calculate the transfer function, namely,

$$
\begin{aligned}
H(i\omega) &= \left. \frac{A_{\text{out}}}{A_{\text{in}}} \frac{(-s\sin(\phi) + \omega\cos(\phi))/(s^2+\omega^2)}{\omega/(s^2+\omega^2)} \right|_{s=i\omega} \\
&= \frac{A_{\text{out}}}{A_{\text{in}}} e^{-i\phi}, \qquad (62)
\end{aligned}
$$

i.e. a constant, independent of ω. Performing an inverse Laplace transform indicates that the corresponding system impulse response is a delta function, namely, $h(t) = (A_{\text{out}}/A_{\text{in}})\delta(t - \phi/\omega)$.

Equation 62 illustrates the important point that evaluation at $s = i\omega$ must take place after the ratio is computed, so that the poles in the Laplace transforms of the sinusoids x and y are removed. In numerical studies making use of the discrete Fourier transform, this evaluation cannot be done after the ratio is computed, which can lead to division by zero. An alternative means for defining the transfer function therefore is via the concept of analytic signals, which have straight-forward numerical approximations and avoid potential division by zero.

Analytic signals are defined in the following manner. Consider the real valued signal $z(t)$ and denote its Fourier transform by $\hat{z}(\xi)$. Define the function

$$\hat{z}_a(\xi) = 2\mathcal{H}(\xi)\,\hat{z}(\xi) \qquad (63)$$

(where $\mathcal{H}$ is the Heaviside step function), which contains only the non-negative frequency components of $\hat{z}(\xi)$. The analytic signal corresponding to z, denoted $z_a(t)$, is a complex-valued function obtained by transforming $\hat{z}_a$ back to the time domain using the inverse Fourier transform, yielding

$$z_a(t) = z(t) + i\mathbb{H}\{z\}(t), \qquad (64)$$

where $\mathbb{H}$ is the Hilbert transform. Properties of Hilbert transforms mean that for input signal $x(t)$ and response signal $y(t)$ of an LTI system, we have that

$$y_a(t) = (h * x_a)(t). \qquad (65)$$

Considering the analytic signals $x_a(t) = -iA_{\text{in}}e^{i\omega t}$ and $y_a(t) = -iA_{\text{out}}e^{i(\omega t - \phi)}$ associated with the input and output signals under consideration, plugging these into (65) yields

$$A_{\text{out}}e^{i(\omega t - \phi)} = A_{\text{in}}e^{i\omega t}H(i\omega). \qquad (66)$$

Equation (66) illustrates the fact that for an input signals of form $e^{i\omega t}$ (called a characteristic function), the response signal is given by $e^{i\omega t}H(i\omega)$, indicating that the output signal is simply a scaling of the input by $H(i\omega)$.

We can solve (66) for the transfer function, namely,

$$H(i\omega) = \frac{A_{\text{out}}}{A_{\text{in}}} e^{-i\phi}, \qquad (67)$$

previously obtained using Laplace transforms. The amplitude $|H| = \left|\frac{A_{\text{out}}}{A_{\text{in}}}\right|$ is often referred to as the gain because it describes how the frequency content in the output signal is amplified in response to the input. And finally, $\phi = -\arg(H)$ is the phase lag, which agrees with that of the 1D Maxwell model considered in the previous section.

As a corollary, if the transfer function is known, we may directly relate the input and output signals. For example, let $x(t) = A\sin(\omega t - \psi)$, with phase ψ, be an input signal and let $H(i\omega) = |H(i\omega)|e^{-i\phi}$ be the transfer function. The analytic input signal is then $x_a(t) = -iAe^{i(\omega t-\psi)}$ and (65) implies that the the analytic output signal is $y_a(t) = H(i\omega)x_a(t)$. The desired output signal $y(t)$ can be recovered by taking the real part of its analytic signal, namely

$$y(t) = |H(i\omega)|A\sin(\omega t - \psi - \phi). \tag{68}$$

In other words, a sinusoidal input function implies a sinusoidal output function, modulated by a phase lag ϕ and amplitude gain $|H|$.

If $\{A_k\}_{k=1}^n, \{\omega_k\}_{k=1}^n, \{\psi_k\}_{k=1}^n$ are sequences of amplitudes, frequencies, and phases, respectively, then a composite input signal can be expressed

$$x(t) = \sum_{k=1}^{n} A_k \sin(\omega_k t - \psi_k). \tag{69}$$

Note that each component is associated with a period $\tau_k = 2\pi/\omega_k$. By superposition, if $\{H(i\omega_k)\}_{k=1}^n$ are (known) associated transfer functions with phase lags $\{\phi_k\}_{k=1}^n$, then the corresponding output signal is given by

$$y(t) = \sum_{k=1}^{n} |H(i\omega_k)|A_k \sin(\omega_k t - \psi_k - \phi_k). \tag{70}$$

In discussion section 6, we illustrate this result for a specific composite input function defining magma reservoir pressure through time and numerically calculated transfer function for resulting surface displacements.

In the sections that follow, we explore numerically how the transfer function links reservoir pressure to surface displacements and strains. Following the notation for the transfer function, we let $\phi\{y(t)\,|\,x(t)\}$ denote the phase lag between the output signal $y(t)$ given the input signal $x(t)$, but drop the argument in curly braces when it is implied via context.

4.3. **Numerical Calculations of the Transfer Function.** The analytic signal corresponding to a real, discrete time-series is implemented in the Python SciPy library (via the python function `scipy.signal.hilbert()`. The transfer function connecting an input signal $x(t)$ to output signal $y(t)$ is computed via the ratio of corresponding analytic signals, from which we can compute phase and amplitude. All scripts are available in the code repository. In practice, there exists an initial spin-up period ($\sim$4 cycles) before solutions settle into a sinusoidal response and it is necessary to compute the transfer function once out of this phase.

In addition to the spin-up phase, the output signal can be shifted to oscillate around a non-zero value, which can complicate the calculation of the phase lag using our numerical techniques. The 1D analysis of the previous section illustrates why this occurs. Specifying the initial condition Equation 49 impacts the evolution of the displacement and stress fields in the following way: suppose $\gamma_0(x) = 0$ for each $x \in [0, L]$. We can simplify the boundary condition Equation 48 by taking $P_0 = \omega = 1$. The sinusoidal pressure imposed at the left boundary along with Equation 47a imply a uniform stress field

$$\sigma(t, x) = \sin t. \tag{71}$$

Integrating Equation 47b yields the viscous strain

$$\gamma(t) = -\frac{1}{\eta}\cos t + \frac{1}{\eta}, \tag{72}$$

and solving Equation 47c for total strain gives the solution

$$\varepsilon(t) = \frac{1}{\mu}\sin t - \frac{1}{\eta}\cos t + \frac{1}{\eta}, \tag{73}$$

which illustrates how the strain response is sinusoidal with a shift of $1/\eta$. Although strain starts initially at 0, it fluctuates around the non-zero value $1/\eta$, corresponding to a volume change (length change in 1D). To avoid this situation, one could specify a different initial viscous strain, i.e. $\gamma_0(x) = -1/\eta$ which would yield a strain response fluctuating around zero. In the 2D problems considered in this work, it is difficult to know a priori the initial viscous strain that would preclude a volume change. Thus to compare the phase-lag response, fields that do not fluctuate around zero must first be shifted to do so. The spin-up phase contributes an exponentially decaying component in the output signal, therefore we calculate approximate phase and amplitude after 4 pressurization cycles.

The sinusoidal pressure forcing we impose at the reservoir wall given by Equation 17a is considered the input signal $P(t)$ for all of our studies. To verify correctness of our numerical methods, we first consider as the output signal the normal component of strain at a single spatial point on the wall, namely $\varepsilon_{rr}(r = a, z = 0, t)$. Because at the reservoir wall the stress-strain relation effectively reduces to a 1D problem at a point, our numeric calculations are verified by comparing our numerical calculations of transfer function amplitude and phase lag against the theoretical stress-strain relationship for a Maxwell material for different forcing periods τ (see Equation 19), as evidenced in Figure 4. In addition we compute the phase lag observed in the vertical component of displacement at Earth's surface $u_z(r = 0, z = D + b, t)$ as well as the transfer function amplitude (gain).

5. Computational Results

Viscoelastic behavior of magma reservoirs is often characterized in terms of deformation of a flat free surface induced by pressurization of a spheroidal reservoir [62, 29, 66]. Even in this relatively simple case, the problem is complex because a large number of control parameters matter and trade off in non-unique ways to generate surface deformation patterns. An additional challenge is that the problem is generally not amenable to analytic analysis such as has been conducted in simplified limits [15, 38, 6].

Having established our computational framework, we will now focus on a specific and relatively unexplored part of this problem here, the frequency dependence of surface deformation. All fixed parameters used in this study are listed in Table 1, unless otherwise noted. In the constant coefficient case studied in Figure 4 (a spherical reservoir in a uniform viscoelastic halfspace), sinusoidal forcing at the reservoir wall results in surface deformation patterns that are simply parameterized in terms of the Deborah number (Equation 59). $De \approx 10$ signifies the onset of viscous response in host rocks, while for $De < 1$ the host rock response is dominantly viscous in the sense that phase lag ϕ between surface deformation is more than halfway to the viscous limit.

We construct constant coefficient models by choosing constant values of elastic parameters μ and λ through spatially averaging the non-constant coefficient calculations (Figure 4, bottom axis). For viscosity we suppose that a forcing period of 1 year yields a surface phase lag of 0.3 rad. From this phase lag we compute the associated Deborah number and solve Equation 28 for viscosity. The resulting constant material parameters are: $\mu = 16.0$ GPa, $\lambda = 16.7$ GPa, $\eta = 2.20 \times 10^{17}\,\mathrm{Pa\,s}$. We can then associate a Deborah number De with a forcing period τ via Equation 28 and examine the transition to a viscous response as a function of forcing

TABLE 1. Parameters used in Applications (unless otherwise noted).

Symbol	Explanation	Value
a	Ellipse semi-major axis	1500 m
b	Ellipse semi-minor axis	1500 m
D	Reservoir depth beneath Earth's surface	3500 m
L_r	Domain length in radial direction	20000 m
L_z	Domain length in vertical direction	20000 m
P_0	Reservoir pressure amplitude	10 MPa
A_D	Dorn parameter	10^9 Pa s
A	Material-dependent constant for viscosity	4.25×10^7 Pa s
E_a	Activation energy	141 kJ/(mol)
R	Boltzmann's molar gas constant	8.314 J/(mol K)
T_c	Reservoir temperature	800°C
T_s	Surface temperature	0°C
α	Geothermal gradient	20°C/km
$\nu_{\min}$	Min Poisson's ratio	0.25
$\nu_{\max}$	Max Poisson's ratio	0.49
$E_{\max}$	Max Young's modulus	4.0×10^{10} Pa
c_1	Parameter in model for E	1.8×10^{10} Pa
c_2	Parameter in model for E	-3.5×10^6 Pa/°C
c_3	Parameter in model for E	4.3×10^9 Pa
s	Parameter in model for E	120 °C
$\bar{T}$	Temperature threshold	924°C

period. In this example $\tau = 1$ yr corresponds to maximum surface displacement that lags behind maximum chamber pressure by ~16 days at similar amplitude to the elastic limit, while $\tau = 10$ yr corresponds to a phase lag of ~1.9 years with ~3× amplitude to the elastic limit.

However, uniform viscosity is a poor approximation to crustal rheology in magmatic regions. To understand what changes with more realistic temperature-dependent viscosity and elastic constants, we also study how pressure forcing period affects ground deformation in the variable coefficient problem outlined in Section 3.3.

Figure 5 left axes show time series of maximum vertical surface displacement and radial strain at the reservoir wall (plotted versus dimensionless time) for several representative forcing periods τ associated with forcing by cyclic pressurization of the chamber (right axes). All quantities are normalized to facilitate comparison of phase lag as a function of forcing period, with amplitudes given in the legend. We see that phase lag differs in magnitude between surface and chamber wall.

Figure 6 plots the spatial variation in vertical and horizontal components of surface displacements u_z, u_r as well as the scalar von Mises stress $\sigma_v = \sqrt{3J_2}$ with J_2 the second deviatoric stress invariant for four positions in the pressure cycle ($\omega = 0, \pi/2, \pi, 3\pi/2$ radians) and three forcing periods. Black and white contours represent level curves of the spatially dependent Deborah number.

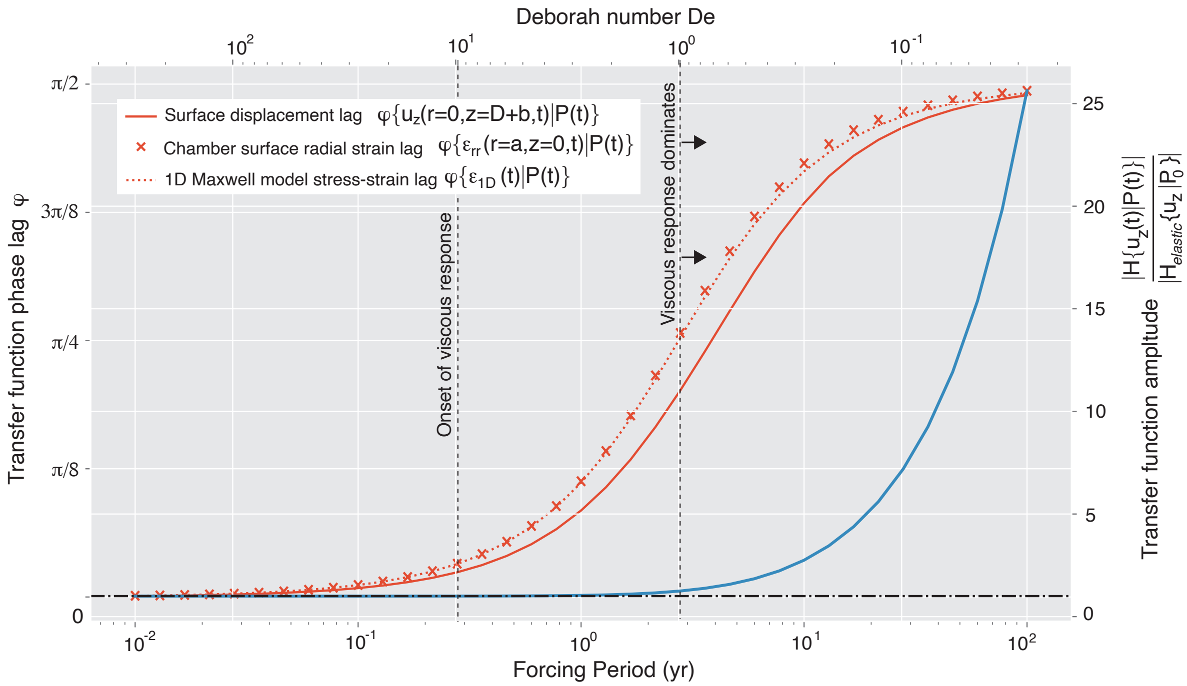

FIGURE 4. Phase lag ϕ of the transfer function between reservoir pressure and radial strain at the reservoir wall ($\phi\{\epsilon_{rr}(r = a, z = 0, t|P(t)\}$, red dashed curve) and vertical displacement at the surface overlying the reservoir ($\phi\{u_z(r = 0, z = D + b, t)|P(t)\}$, solid red curve). Crosses come from the 1D analytic prediction (Equation 59). Right axis and blue curve plot the amplitude of the transfer function $|H\{u_z(r = 0, z = D + b, t|P(t)\}|$ normalized by the transfer function amplitude in a purely elastic limit (which uses the same averaged elastic coefficients but with $\eta = 1 \times 1^{34}$ making viscous effects negligible). Upper x axis is the Deborah number, lower x-axis dimensionalizes into period of sinusoidal pressure forcing using $\eta = 2.20 \times 10^{17}$ Pas, $\lambda = 16.7$ GPa and $\mu = 16.0$ GPa. Vertical dashed lines correspond to threshold Deborah numbers associated with onset of viscous response in host rocks.

Finally, Figure 7 shows the transfer function phase $\phi\{u_z(r = 0, z = D + b, t) \,|\, P(t)\}$ and normalized amplitude $|H\{u_z(r = 0, z = D + b, t) \,|\, P(t)\}|/|H_{elastic}\{u_z(r = 0, z = D + b) \,|\, P_0\}|$ for a sweep through pressure forcing period τ. The elastic normalization $H_{elastic}$ is computed for each temperature separately, due to temperature dependence of elastic parameters E and ν (non-constant coefficient corrections to the known spherical cavity in half space elastic solution [71]). Transfer function results are computed for three choices of reservoir temperature $T_c = 800, 900, 1000°$C in Figure 7. The simulations are carried out at 37 logarithmically-spaced forcing periods between 0.01yr and 100yr. For each forcing period and reservoir temperature, we compute the transfer function phase and amplitude over 10 complete pressurization cycles. Because of computational burden associated with the highest reservoir temperature of 1000°C (Figure 2) that lead to very small Deborah numbers, we set a maximal effective temperature of 900°C for computing material parameters in this case. We also perform an additional

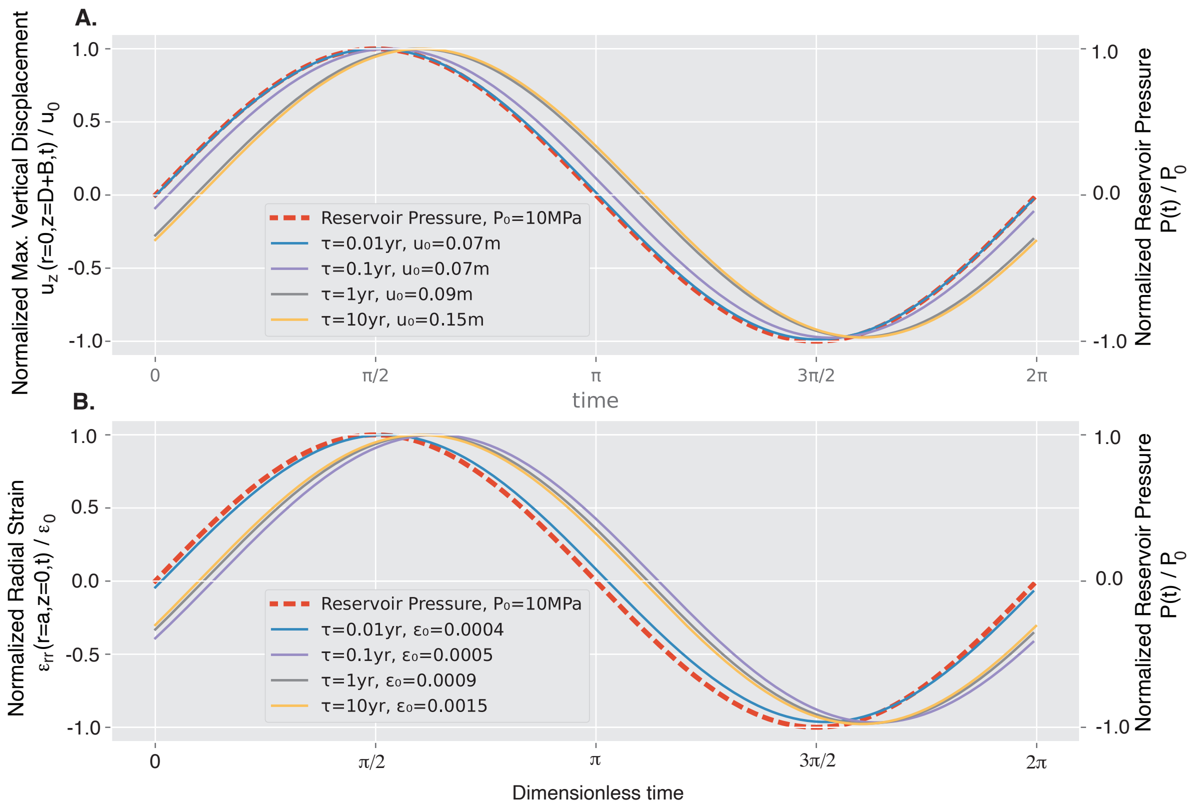

FIGURE 5. Temporal evolution (time non-dimensionalized by τ) associated with non-constant coefficient simulations at select forcing periods. Colored curves correspond to different forcing periods and normalization amplitudes u_0, ϵ_0, dashed curves show pressure normalized by P_0. **A.** Normalized maximum vertical surface displacement. In dimensional time, peak vertical surface displacement for $\tau = 0.01, 0.1, 1, 10$ years occurs 10.0 min, 12.7 hr, 17.6 days, and 6.3 months after peak reservoir pressure, respectively, associated with phase lags $\phi\{u_z(r = 0, z = D + b, t|P(t)\} = 0.012, 0.091, 0.303$ and 0.331 radians. **B.** Normalized radial strain at the cavity wall, illustrating that phase offset of deformation from pressure forcing varies spatially through the domain.

mesh refinement in space to mitigate poor resolution at longer forcing periods for the 1000°C reservoir.

In contrast to the constant coefficient case, Figures 5-7 demonstrate that temperature dependent material parameters strongly impact the frequency dependence of system viscoelastic response. Most pronounced is a saturation of phase lag at ~ 0.3 radians and muted amplification of displacements relative to the constant coefficient case. As evidenced by the large σ_v (which measures deviatoric shear stress magnitude), viscous effects are confined near the reservoir wall. This results in more pronounced mechanical lag at the reservoir wall than at the surface (Figure 5) and concentration of shear stress σ_v through the cycle in a narrow aureole around the chamber (Figure 6).

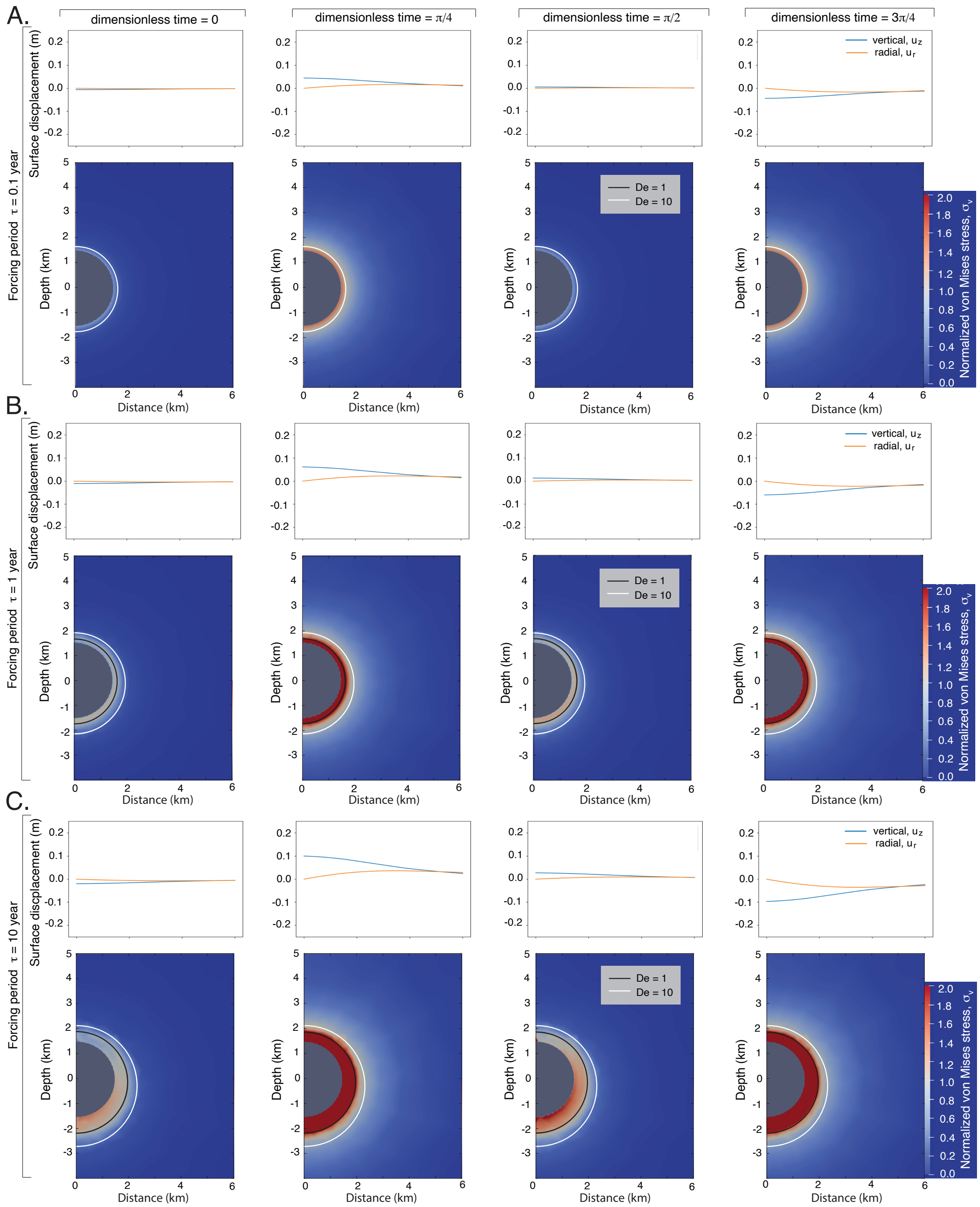

FIGURE 6. Spatial pattern of surface displacements u_z, u_r (top lines) and subsurface distribution of von Mises stress σ_v (bottom colors, normalized by $P_0 = 10$ MPa) for dimensionless times $0, \pi/4, \pi/2, 3\pi/4$ during a pressure cycle. Black contour is $De = 1$, white contour is $De = 10$, illustrating that a local Deborah number contour approximates the spatial region of elevated deviatoric stress and viscous strain around the chamber. **A.** Forcing period $\tau = 0.1$ yr, max $\sigma_v = 20.9$ MPa. **B**. Forcing period $\tau = 1$ yr, max $\sigma_v = 42.2$ MPa. **C.** Forcing period $\tau = 10$ yr, max $\sigma_v = 100.7$ MPa. Supplemental movies S1-S3 show time evolution of these simulations in more detail.

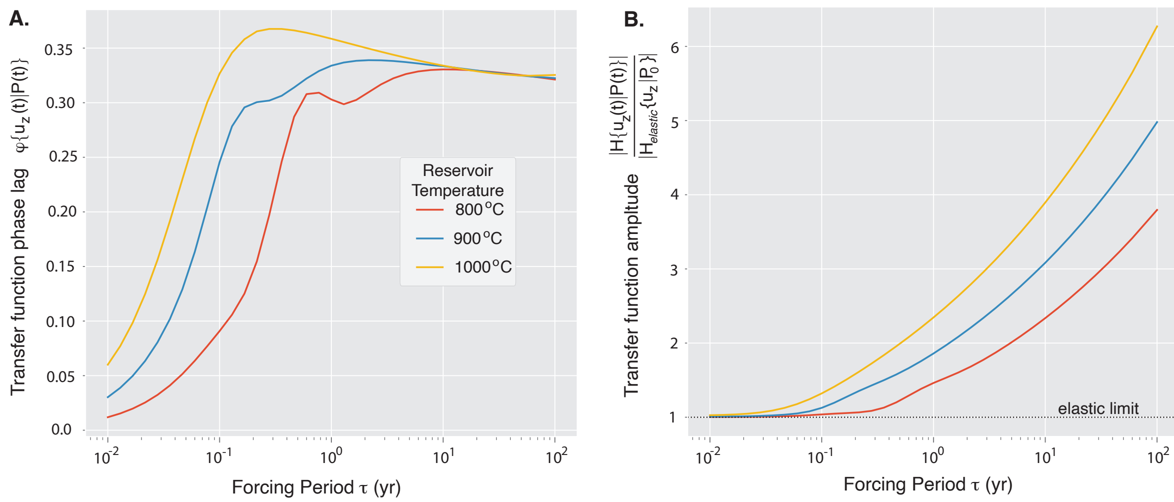

FIGURE 7. Transfer function between reservoir pressure and maximum vertical surface displacement $H\{u_z(r=0, z=D+b, t)|P(t)\}$ as a function of sinusoidal pressure forcing period τ. Colored curves correspond to different reservoir temperatures, each case assumes surface temperature $T_s = 0°\text{C}$ and geothermal gradient $\alpha = 20$ C/km. **A.** Phase lag $\phi\{u_z(r=0, z=D+b, t)|P(t)\}$ (in radians). **B.** Amplitude $|H\{u_z(r=0, z=D+b, t)|P(t)\}|$ normalized by the corresponding variable coefficient elastic case at each temperature. For the three reservoir temperatures explored here, $|H_{elastic}\{u_z(r=0, z=D+b)|P_0\}| = 6.509 \times 10^{-9}, 6.822 \times 10^{-9}, 7.163 \times 10^{-9}$ m/Pa for $T_c = 800, 900, 1000°\text{C}$ respectively.

The strong spatial variability in material parameters now implies a spectrum of Maxwell relaxation times as has been noted in other studies, [30], and hence spatially variable Deborah number. Nonetheless, we see that a local value of De still characterizes the region experiencing significant viscous strain for each forcing period. Figure 6 shows that $De \approx 10$ effectively bounds the region experiencing significant von Mises stress, and hence viscous strain, in excess of chamber overpressure P_0, with $De = 1$ once again a measure of the viscous region centroid. For small forcing periods the viscous region is significantly reduced ($De = 1$ does not appear for $\tau = 0.1$ year forcing period). Both contours are asymmetric with depth due to the geothermal gradient. To isolate viscous effects, the transfer amplitudes for Figure 7 are normalized using the variable coefficient elastic limit. That is, elastic parameters are computed using a thermal profile but viscosity $\eta = 1 \times 10^{34}$Pa·s. Then this variable coefficient elastic problem is simulated and a transfer function $H_{elastic}$ is computed from the output.

The transfer function curves in Figure 7 have more complex structure than their constant coefficient counterpart in Figure 4. First, the phase lag $\phi\{u_z(r=0, z=D+b, t)\,|\,P(t)\}$ is non-monotonic, with two local maxima superimposed on a sigmoidal increase from 0 to ~ 0.3 radians over three orders of magnitude in forcing period. The second of these is a global maximum for the range of forcing periods we explored (100 years maximum), and appears to reflect the finite region around the chamber in which viscous strains occur. Increasing the reservoir temperature from 800°C to 1000°C shifts this global maximum as well as the sigmoidal uptick in phase lag to shorter periods, which suggests that the local maxima are due in part to an expanded viscous shell around the reservoir (i.e., larger region where $De < 10$). As will be discussed in the next section, we speculate that a non-monotonic phase lag at longer periods occurs because larger regions of the domain begin to contribute to the surface displacements. We expect that the shape of this phase lag curve as metric of viscoelastic response likely depends on spatial rheologic structure, boundary conditions, and chamber geometry, although a parameter exploration is out of the scope of this study.

The apparent global maximum seen in the phase lag in Figure 7 is not mirrored by the amplitude of displacements. Relative to the elastic limit transfer function amplitude show a continuous increase in maximum displacements at increasing τ, mirrored by the spatial pattern of u_z and u_r in Figure 6. There is an inflection point that corresponds to the local minimum in ϕ for the lower reservoir temperatures, but viscous amplification is otherwise a monotonically increasing function of τ, with amplification factors at 100 yr forcing period $\sim$3.8$\times$, $\sim$5$\times$ and $\sim$6.3$\times$ for 800°C, 900°C, and 1000°C chamber temperatures. At small τ the amplification factor is asymptotic to the variable coefficient elastic limit (dashed line) in all cases.

6. Discussion

This work makes two primary contributions. First, we develop a rigorous numerical framework based on a high-order finite element method for the computation of deformation and stress around axisymmetric magma reservoirs. Second, we study a particular problem - sinusoidal pressurization/depressurization of a spherical reservoir in a half-space - and demonstrate how surface deformation patterns are frequency dependent. This section is organized into a discussion associated with each contribution as they relate to the phenomenology of viscoelastic deformation around volcanoes.

6.1. **Computational Considerations for Time-evolving Magmatic Systems.**

Viscoelastic deformation of volcanoes has been studied analytically and numerically by numerous authors [33, 63, 70]. However, we are unaware of a systematic analysis of the numerical and computational issues associated with this problem. As volcanic deformation datasets become better resolved in space and time, and as magma reservoir models are generalized to include more physical processes over an increasing range of timescales, neglecting these numerical and computational considerations is likely to be a major factor limiting scientific progress.

We derived conditions on the time step, which guarantees stability of the aging law, and showed that the numerical solution converges to the exact solution at the theoretical rates of convergence in both space and time. However, in practice, even these 2D simulations are computationally expensive because a system of equations (the discretized equilibrium equation) must be solved at each time step, and this constitutes the bulk of the computational load. We perform a direct solve of the system while it is still possible to hold the matrix factorization in system memory. For larger problems (e.g. in 3D or with larger domains sizes or if a finer spatial resolution is required), matrix-free iterative methods on parallel machines would be necessary [9]. Furthermore, if the relevant time scale of interest is the forcing period τ, which can be much longer than the minimum viscous relaxation time η/μ (so that $De \ll 1$), the problem can become arbitrarily numerically stiff: very small time steps are required for numerical stability, much smaller than that required to accurately resolve the sinusoidal pressure forcing.

To address this corresponding computational burden, an implicit time stepping scheme (such as backward Euler) would need to be applied, or alternative schemes such as splitting algorithms [8]. For problems in which total strains are large (e.g., dominated by viscous flow) it may also be advantageous to reformulate the governing equations in terms of split viscous and elastic strain rates (rather than strains), as is commonly done in mantle dynamics models [50]. A disadvantage of this approach is that elastic stresses are less explicitly resolved, which is not acceptable for the present application. Still, one drawback of our method is that it is not robust in the incompressible limit ($\nu = 0.5$). More sophisticated locking-free mixed finite element techniques [21] could be employed to solve the equilibrium equations stably in the incompressible limit, a potential necessity in fully coupled fluid-solid magmatic models. Codes developed for large-scale geodynamic applications commonly include compressible fluid but incompressible solid mechanics [31]. This difference in approach implies that extensions of our computational framework to a broader range of problems might require further numerical developments.

The inclusion of boundary tractions (to represent background tectonic stress, for example) can be explored here directly by setting specific values of the boundary data. Topography at the surface or at depth can be included by modifying the axisymmetric domain geometry. Complex time-evolving forcing can be included so long as the highest frequency is resolved by the timestep, as we demonstrate in the next section. But highly multiscale time evolution, such as might be expected for pressure at the reservoir wall over eruption cycles [10,], may require adaptive time-stepping techniques to integrate efficiently through regions of both slow and fast evolution. Similar challenges arise in the modeling of long-term earthquake cycles [16], and similar timestepping approaches could be leveraged for simulating volcanic activity.

6.2. **Frequency Dependent Magmatic Deformation.** We have studied here a magma chamber problem that, while simplified in some respects, has a strong basis in past observations and represents a template for future advances. In the elastic limit, corrections for less idealized geometry and material heterogeneity are known [61], and elastic parameter trade-offs have been explored to some extent [12, 56]. But viscoelastic behavior is far less well understood. Case studies have demonstrated important trade-offs in geometry, constitutive law, and thermal state, as well as complications associated with time-dependent rheology [25, 63, 29, 30]. But general time-dependence introduces significant complexities.

The cyclic forcing studied here represents a powerful framework to explore phenomenology of transient magma chamber deformation. While magma pressure histories are not generally sinusoidal, linear viscoelasticity (in any form, not just the Maxwell model) implies that arbitrary forcing histories may be constructed through appropriate superposition. The analysis of section 4.2 details how knowledge of the transfer function can be used to relate such composite signals. We illustrate this approach with three examples.

First, consider a reservoir pressure history (the input signal) given by the 2τ-periodic rectangular pulse of unit width

$$P(t) = P_0 \left(\mathcal{H}(t) - \mathcal{H}(t-1)\right), \tag{74}$$

with $\tau > 1$. The complex Fourier series representation for $P(t)$ can expressed as

$$P(t) = \sum_{n=-\infty}^{\infty} c_n e^{i\omega_n t}, \tag{75}$$

where $\omega_n = n\pi/\tau$ and the complex Fourier coefficients are given by

$$c_n = P_0 \frac{1}{\tau\omega_n} e^{-i\omega_n/2} \sin(\omega_n/2). \tag{76}$$

Then the output signal $y(t)$ can be expressed in terms of its Fourier series

$$y(t) = \sum_{n=-\infty}^{\infty} d_n e^{i\omega_n t} \tag{77}$$

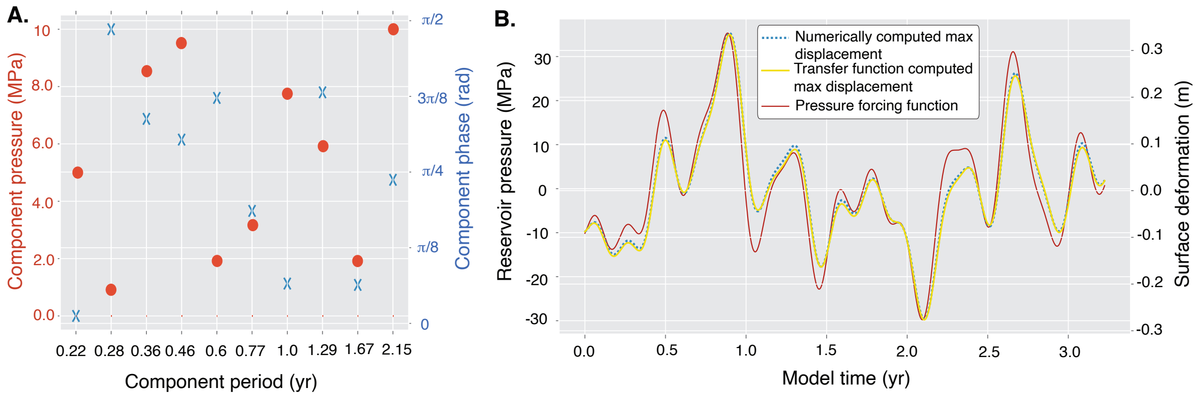

FIGURE 8. **A.** Amplitudes and phases of input pressure signal, Equation (69). **B.** Input pressure timeseries (red curve) along with numerically computed maximum surface displacement (dashed blue curve) and analytic prediction based on the transfer function, Equation 70.

with coefficients

$$d_n = H(i\omega_n)c_n, \tag{78}$$

i.e. the coefficients of the input signal, scaled by the transfer function H. This example demonstrates that sequences of impulsive pressure changes (such as eruptions) that are non-harmonic in time can still be characterized with the framework developed here.

As a second example, if the pressure history is given by a unit impulse at $t = t_0$, namely

$$P(t) = P_0\delta(t - t_0), \tag{79}$$

then Equation 60 implies that the output signal is simply

$$y(t) = h(t - t_0), \tag{80}$$

i.e. the system impulse response. This pressure history represents a simple model for sudden pressure perturbation [62]. The implied ground deformation in this case is the impulse response function of the magma chamber/host rock system.

These examples demonstrate the transfer function approach in a forward modeling framework. Frequency-domain inversion of magmatic pressure histories from ground motions, a common scenario since reservoir pressure is generally unknown, by extension involves seeking weights for the forcing periods represented in Figure 7 to match general time-dependent deformation data. To demonstrate this explicitly, we present a third example in which we construct a non-harmonic input pressure signal by summing sinusoids at a subset of forcing frequencies explored in Figure 7 with random phase and amplitude (assuming an 800°C chamber representing a lower bound to the viscoelastic response) corresponding to Equation 69. Weights and phases are displayed in Figure 8.A. We compute the output signal from Equation 70 and show that the predicted surface deformation matches the numerically computed output (Figure 8.B). Numerical displacements shown here are after a spin-up to make sure the output is in steady state with the input.

Outputs of interest are thus easily found given knowledge of the transfer function. Of course, in reality this transfer function is unknown and would need to be computed as part of an inversion. Further studies will be needed to quantify the variability of the transfer function as control parameters are varied. This will determine the sensitivity of phase lag and amplitude spectrum to rheologic model, chamber geometry, and temperature structure.

Figure 8.B also demonstrates the non-trivial impact of frequency-dependent phase lag and amplitude on ground deformation. Even though a relatively narrow range of frequencies is present in the forcing function ($2\pi/\omega_k = \tau_k \sim 0.2 - 2$ yr in equation 69), we see that shorter period forcing generates in-phase ground displacements, while longer period ground motions are out of phase with chamber pressure. These effects would be amplified for warmer (more viscous) host rocks and longer forcing periods, and should be observable in geodetic timeseries with several day resolution (phase lag associated with 1 year forcing period from Figure 7 is ~ 18 days). We also see that the ground displacement amplitude is a function of frequency as predicted from the transfer function. It is not simply proportional to the pressure as would be expected from elasticity [48], and reflects the amplitudes of each component period shown in fig 8.A scaled by the transfer function.

An interesting challenge implied by our analysis with respect to observations however is how to find initial conditions. Our time-dependent steady-state (purely oscillatory) implicitly starts from a unstressed state, but as illustrated through 1D analysis (Section 4) the initial strain determines the equilibrium position around which steady viscoelastic oscillations occur. In the 2D variable coefficients case the choice of initial strain that will result in a particular chamber size (or geometry) is less trivially found - equilibrium magma chamber volume is not an independent parameter but rather a model outcome. From a geophysical perspective, this implies that absolute stress histories are needed to interpret general surface displacement timeseries at volcanoes, and could play an important role in eruption cycles as it does for earthquake cycles [17].

Another important implication of this model is that the volume of crustal rock around the chamber that experiences viscous strain over a chamber pressure cycle depends on the frequency of forcing. As demonstrated by Figure 4, $De = 10$ effectively marks the onset of viscous host response to cycling pressure forcing. Figure 6 extends this to variable coefficients, suggesting that $De \approx 10$ effectively bounds the region in which significant deviatoric shear stresses (as measured by σ_v in excess of P_0) occur.

We suggest that the frequency-dependent $De \approx 10$ contour represents an effective outer edge to the viscoelastic "shell" at a given frequency of forcing. This shell has been largely considered fixed in size by previous models for viscoelastic magma chamber mechanics [15, 36, 38, 13, 62, 44]. Our model demonstrates that viscoelastic shell size even for a steady temperature distribution dependents on the time history of reservoir stress - like equilibrium reservoir size, it is a transient model output.

6.3. **Implications for Transcrustal Magmatic Systems.** Magma reservoirs that feed volcanic eruptions likely sit near the top of transcrustal magma transport networks characterized by high temperatures and partial melt [65,]. Some of this magma accumulates episodically into high melt fraction reservoirs such as we model here. But it is to be expected that, as transcrustal magma transport networks mature, a significant fraction of the crust is heated and remains hot for extended periods of time. What are the implications of this rheological structure for ground deformation?

We can begin to answer this question by noting that the bulk crustal rheology of magma storage zones as expressed by surface deformation depends on frequency of forcing, as it does on the spatial structure of melt and temperature [52]. This has been long recognized for crustal rheology in other settings [55, 41,]. But volcanoes offer a particularly interesting case for exploring crustal rheology, because different histories of heating – all else equal – will

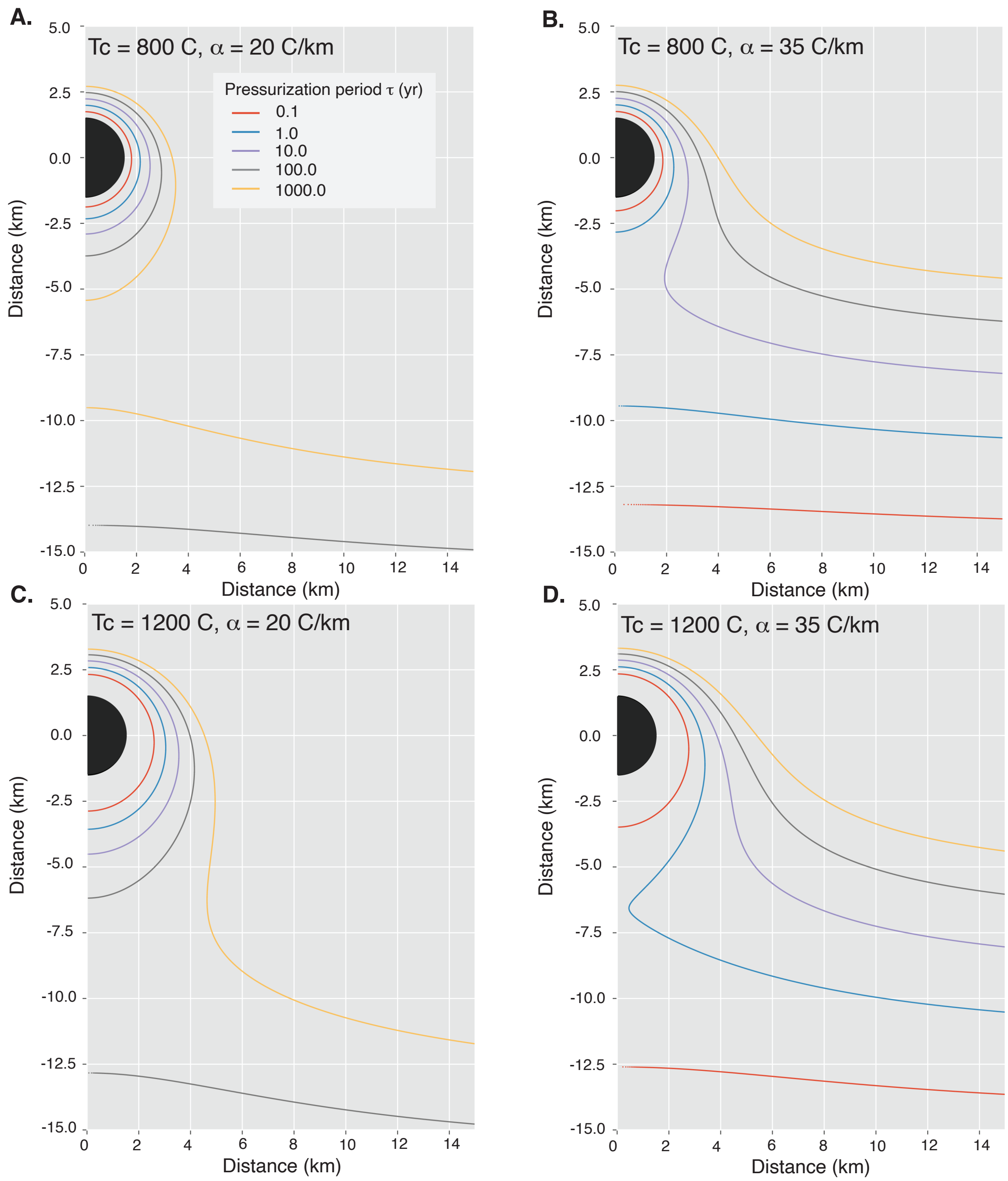

FIGURE 9. Spatial regions associated with a local Deborah number $De = 10$ for varying periods τ of the chamber pressure forcing function (colored curves), illustrating end member thermal regimes. Magma reservoir is black semi-circle in all panels. **A.** Reservoir temperature $T_c = 800°C$ with geothermal gradient $\alpha = 20°C/km$. **B.** Reservoir temperature $T_c = 800°C$ with geothermal gradient $\alpha = 35°C/km$. **C.** Reservoir temperature $T_c = 1200°C$ with geothermal gradient $\alpha = 20°C/km$. **D.** Reservoir temperature $T_c = 1200°C$ with geothermal gradient $\alpha = 35°C/km$.

have distinct deformation frequency response curves (transfer functions) in the frequency band where geophysical observations are routinely made.

Figure 9 plots the $De = 10$ contour representing onset of viscous mechanical response for different pressurization periods, from 0.1 to 1000 years. We then consider end member steady state thermal regimes: chamber boundary temperature of $T_c = 800°\mathrm{C}$ and $1200°\mathrm{C}$, and geothermal gradient of $\alpha = 20°\mathrm{C/km}$ and $35°\mathrm{C/km}$. In the cold extreme (Figure 9**A**), we see that viscoelastic behavior is confined to a shell around the chamber in all but 1000 year forcing. This is consistent with commonly used models of isolated magma chambers. At long forcing periods however the mid/lower crust is activated and starts to creep, defining a mid-crustal brittle-ductile transition that depends on background geothermal gradient. In the hot extreme (Figure 9**D**), we see that viscoelastic response of the near-chamber region extends continuously into the mid-crust for forcing periods as low as 10 years. This defines a spatially coherent viscous domain induced by magmatic heating [39,], activated by long-period forcing.

While we leave further exploration of this to future work, we note that some of the structure seen in phase lag variations in Figure 7 likely reflect changes to the shape as well as volume of the viscous near-chamber region. It is notable that significant sensitivity of viscoelastic response to forcing period and variations in thermal structure in the $0.1 - 10$ year range, where geodetic observations are increasingly common. Because magma transport is unsteady at many scales, ground deformation in volcanic regions will likewise include contributions from viscoelastic deformation defining the crustal thermo-rheologic footprint of magmatism on a range of timescales.

Appendix A. Verification via Convergence Tests

We verify the accuracy of our numerical method using the method of manufactured solutions (MMS) [57] and explain this technique in the context of the dimensional problem (computationally we solve the non-dimensionalized problem). The MMS verification technique lets us choose arbitrary solution fields $u^*(r,z,t), C^*(r,z,t)$ to act as exact solutions to any initial-boundary-value problem, even those without a known analytic solution) necessary for measuring convergence. The key point is that u^* and C^* satisfy the governing equations and boundary conditions with particular choices of source terms and boundary data which we detail in this section.

We choose a manufactured solution to the initial-boundary-value problem Equation (1a),(4)-(8) based on the well-known solution to the pressurized magma cavity problem in an elastic half-space [48, 61] given by

$$\mathbf{u}_e = \frac{P_0 a^3}{4\mu(r^2+z^2)^{3/2}} \begin{bmatrix} r \\ z \end{bmatrix}. \tag{81}$$

which satisfies the reservoir pressure conditions Equations (17a)-(17b). Define the manufactured solutions u^*, C^* by

$$u^*(r,z,t) = (2 - e^{-t})\mathbf{u}_e, \tag{82}$$

$$C^*(r,z,t) = (1 - e^{-t})\boldsymbol{E}\underline{\boldsymbol{\varepsilon}}(\mathbf{u}_e), \tag{83}$$

which satisfies equilibrium and specifies all boundary data. It does not however satisfy the aging law, and to correct for this discrepancy a source term is added, namely

$$\underline{\dot{\boldsymbol{C}}} = \boldsymbol{E}\boldsymbol{A}\underline{\boldsymbol{\sigma}} + \boldsymbol{G}. \tag{84}$$

TABLE 2. Parameters used in Convergence Tests and their Symbols.

Symbol	Explanation	Value
a	Ellipse semi-major axis	4 km
b	Ellipse semi-minor axis	4 km
D	Reservoir depth beneath Earth's surface	5 km
L_r	Domain length	10 km
L_z	Domain depth	10 km
μ	shear modulus	0.5 GPa
λ	Lamé's first parameter	4 GPa
η	Viscosity	0.5 GPa-s
P_0	Chamber Pressure	10 MPa

TABLE 3. Spatial convergence data, measured with respect to the discrete L^2-norm, for a single time step of $\Delta t = 10^{-7}$ using polynomials of degree 3.

h	$\lVert\underline{\boldsymbol{C}} - \underline{\boldsymbol{C}}_h\rVert$	$\underline{\boldsymbol{C}}$-rate	$\lVert\mathbf{u} - \mathbf{u}_h\rVert$	$\mathbf{u}$-rate
$h/2$	5.25×10^{-9}		1.84×10^{-8}	
$h/4$	7.17×10^{-10}	2.87	1.31×10^{-9}	3.81
$h/8$	9.13×10^{-11}	2.97	8.41×10^{-11}	3.96
$h/16$	1.14×10^{-11}	3.00	5.24×10^{-12}	4.00

TABLE 4. Temporal convergence data measured at point $(\tilde{A}, 0)$ under the discrete L^2-norm.

Δt	$\lVert\underline{\boldsymbol{C}} - \underline{\boldsymbol{C}}_h\rVert$	$\underline{\boldsymbol{C}}$-rate	$\lVert\mathbf{u} - \mathbf{u}_h\rVert$	$\mathbf{u}$-rate
$\Delta t/2$	1.75×10^{-1}		1.18×10^{-6}	
$\Delta t/4$	8.85×10^{-2}	0.99	5.96×10^{-7}	0.99
$\Delta t/8$	4.46×10^{-2}	0.99	3.01×10^{-7}	0.99

Here, the source term $\boldsymbol{G}$ is determined from the manufactured solutions to be

$$\boldsymbol{G} = e^{-t}\sigma^* - \frac{\mu}{\eta} \operatorname{dev} \sigma^*, \tag{85}$$

where σ^* is the manufactured stress and can be obtained by computing

$$\sigma^* = \boldsymbol{E}\underline{\boldsymbol{\varepsilon}}(\mathbf{u}_e). \tag{86}$$

All parameters used are given in Table 2. Table 3 shows the spatial errors $\lVert\underline{\boldsymbol{C}} - \underline{\boldsymbol{C}}_h\rVert$ and $\lVert\mathbf{u} - \mathbf{u}_h\rVert$ when computing approximations to C^* and u^* after a single time step, using a stable step size of 10^{-7} and the discrete L^2-norm. Successive mesh refinements are made using polynomials of degree 3 as a basis for the FEM space. Convergence rates agrees with FEM theory which predict a convergence rate of $p+1$ for u^* and p for C^* when polynomials of degree p are used [40]. The same convergence pattern is observed for polynomials with degree greater than 3 except that the L^2-error drops below machine precision leading to round-off error in the rate computation.

To measure the convergence in the temporal domain we select a single point in space and perform successive mesh refinements in time. Table 4 shows that both $\underline{\boldsymbol{C}}$ and $\mathbf{u}$ exhibit rate-1 temporal convergence, consistent with forward Euler.

The benefit of convergence tests based on the MMS technique is that solutions can be manufactured for problems with more physical complexities, as opposed to relying on simple problems with known analytic solutions such as those highlighted in [33]. With MMS, rigorous convergence can be obtained at the exact theoretical rate, a desirable outcome for high-order numerical methods. That being said, the MMS technique requires making specific choices for source and boundary data, which can sometimes alter the underlying physics of interest. Thus code verification can benefit further from community based efforts, as done extensively in the earthquake community [28, 18]. In community benchmarking, all mathematical details of a problem are specified and different modeling groups compare code output and seek quantitative comparisons. These exercises can be done for problems with or without a known analytic solution; the simple problems detailed in [33] (including the homogeneous, viscoelastic "Del Negro" model, [14]) could serve as the first benchmark problem statements for the magma reservoir community code verification efforts, with further benchmark problems containing increasingly physical and/or geometrical properties where analytic solutions are not known.

Open Research

Software consists of Python code developed on top of the free and open source multi-physics library NGSolve [60] and the accompanying mesh generator [59]. All source code is freely available in the public repository [23].

Acknowledgments

CR, BAE and LK were supported by NSF grant EAR- 2036980. LK also acknowledges NSF grant 1848554. BL and JG were supported by NSF grant DMS-1912779. This work benefited from access to the University of Oregon high performance computer Talapas and the COEUS cluster at the Portland Institute for Computational Science. We thank James Hickey, an anonymous reviewer, and the editor for comments and suggestions that improved the paper considerably. The authors acknowledge useful discussions with Yang Liao ad Ben Holtzman.

References

[1] K. L. Allison and E. M. Dunham. Earthquake cycle simulations with rate-and-state friction and power-law viscoelasticity. *Tectonophysics*, 733:232–256, 2018.

[2] K. A. Anderson and P. Segall. Physics-based models of ground deformation and extrusion rate at effusively erupting volcanoes. *Journal of Geophysical Research Solid Earth*, 116(B7):1–20, 2011.

[3] R. R. Bakker, M. Frehner, and M. Lupi. How temperature-dependent elasticity alters host rock/magmatic reservoir models: A case study on the effects of ice-cap unloading on shallow volcanic systems. *Earth and Planetary Science Letters*, 456:16–25, 2016.

[4] G. Berrino, G. Corrado, G. Luongo, and B. Toro. Ground deformation and gravity changes accompanying the 1982 Pozzuoli uplift. *Bulletin volcanologique*, 47(2):187–200, 1984.

[5] B. A. Black and M. Manga. Volatiles and the tempo of flood basalt magmatism. *Earth and Planetary Science Letters*, 458:130–140, 2017.

[6] M. Bonafede, M. Dragoni, and F. Quareni. Displacement and stress fields produced by a centre of dilation and by a pressure source in a viscoelastic half-space: application to the study of ground deformation and seismic activity at Campi Flegrei, Italy. *Geophysical Journal International*, 87(2):455–485, 1986.

[7] R. Bürgmann and G. Dresen. Rheology of the lower crust and upper mantle: Evidence from rock mechanics, geodesy, and field observations. *Annual Review of Earth and Planetary Sciences*, 36:531–567, 2008.

[8] J. M. Carcione and G. Quiroga-Goode. Some aspects of the physics and numerical modeling of biot compressional waves. *Journal of Computational Acoustics*, 03(04):261–280, 1995.

[9] A. Chen, B. Erickson, and J. Kozdon. Matrix-free methods for summation-by-parts finite difference operators on GPUs. *submitted*, 2022.

[10] S. Cianetti, C. Giunchi, and E. Casarotti. Volcanic deformation and flank instability due to magmatic sources and frictional rheology: the case of mount etna. *Geophysical Journal International*, 191:939–953, 2012.

[11] J. Crozier and L. Karlstrom. Evolving magma temperature and volatile contents over the 2008–2018 summit eruption of kīlauea volcano. *Science Advances*, 8(22):eabm4310, 2022.

[12] G. Currenti and C. A. Williams. Numerical modeling of deformation and stress fields around a magma chamber: Constraints on failure conditions and rheology. *Physics of the Earth and Planetary Interiors*, 226:14–27, 2014.

[13] W. Degruyter and C. Huber. A model for eruption frequency of upper crustal silicic magma chambers. *Earth and Planetary Science Letters*, 403:117–130, 2014.

[14] C. Del Negro, G. Currenti, and D. Scandura. Temperature-dependent viscoelastic modeling of ground deformation: Application to Etna volcano during the 1993–1997 inflation period. *Physics of the Earth and Planetary Interiors*, 172(3):299–309, 2009.

[15] M. Dragoni and C. Magnanensi. Displacement and stress produced by a pressurized, spherical magma chamber, surrounded by a viscoelastic shell. *Physics of the Earth and Planetary Interiors*, 56(3):316–328, 1989.

[16] B. A. Erickson and E. M. Dunham. An efficient numerical method for earthquake cycles in heterogeneous media: Alternating subbasin and surface-rupturing events on faults crossing a sedimentary basin. *Journal of Geophysical Research: Solid Earth*, 119(4):3290–3316, 2014.

[17] B. A. Erickson, E. M. Dunham, and A. Khosravifar. A finite difference method for off-fault plasticity throughout the earthquake cycle. *Journal of the Mechanics and Physics of Solids*, 109:50–77, 2017.

[18] B. A. Erickson, J. Jiang, M. Barall, N. Lapusta, E. M. Dunham, R. Harris, L. S. Abrahams, K. L. Allison, J. P. Ampuero, S. Barbot, C. Cattania, A. Elbanna, Y. Fialko, B. Idini, J. E. Kozdon, V. Lambert, Y. Liu, Y. Luo, X. Ma, M. B. Mckay, P. Segall, P. Shi, M. van den Ende, and M. Wei. The community code verification exercise for simulating sequences of earthquakes and aseismic slip (seas). *Seismological Research Letters*, 91:874–890, 2020.

[19] A. Ern and J.-L. Guermond. Finite elements i, 2021.

[20] J. Golden and G. Graham. *Boundary Value Problems in Linear Viscoelasticity.* Springer-Verlag, 1 edition, 1988.

[21] J. Gopalakrishnan and J. Guzmán. A second elasticity element using the matrix bubble. *IMA J. Numer. Anal.*, 32:352–372, 2012.

[22] J. Gopalakrishnan and J. E. Pasciak. The convergence of V-cycle multigrid algorithms for axisymmetric Laplace and Maxwell equations. *Mathematics of Computation*, 75:1697–1719, 2006.

[23] J. Gopalakrishnan and C. Rucker. Bitbucket: `magmaxisym`. `https://bitbucket.org/jayggg/magmaxisym/src/master/`, 2022. Repository with python drivers for computing dynamics of viscoelastic medium surrounding an axisymmetric magma cavity using NGSolve.

[24] J. Gottsmann and H. Odbert. The effects of thermomechanical heterogeneities in island arc crust on time-dependent preeruptive stresses and the failure of an andesitic reservoir. *Journal of Geophysical Research: Solid Earth*, 119:4626–4639, 2014.

[25] R. Grapenthin, B. G. Ófeigsson, F. Sigmundsson, E. Sturkell, and A. Hooper. Pressure sources versus surface loads: Analyzing volcano deformation signal composition with an application to hekla volcano, iceland. *Geophysical Research Letters*, 37(20), 2010.

[26] P. Gregg, S. De Silva, and E. Grosfils. Thermomechanics of shallow magma chamber pressurization: Implications for the assessment of ground deformation data at active volcanoes. *Earth and Planetary Science Letters*, 384:100–108, 2013.

[27] P. Gregg, S. De Silva, E. Grosfils, and J. Parmigiani. Catastrophic caldera-forming eruptions: Thermomechanics and implications for eruption triggering and maximum caldera dimensions on earth. *Journal of Volcanology and Geothermal Research*, 241:1–12, 2012.

[28] R. A. Harris, M. Barall, R. Archuleta, E. M. Dunham, B. Aagaard, J. P. Ampuero, H. Bhat, V. Cruz-Atienza, L. Dalguer, P. Dawson, S. Day, B. Duan, G. Ely, Y. Kaneko, Y. Kase, N. Lapusta, Y. Liu, S. Ma, D. Oglesby, K. Olsen, A. Pitarka, S. Song, and E. Templeton. The SCEC/USGS dynamic earthquake rupture code verification exercise. *Seismological Research Letters*, 80:119–126, 2009.

[29] M. Head, J. Hickey, J. Gottsmann, and N. Fournier. The influence of viscoelastic crustal rheologies on volcanic ground deformation: Insights from models of pressure and volume change. *Journal of Geophysical Research: Solid Earth*, 124(8):8127–8146, 2019.

[30] M. Head, J. Hickey, J. Gottsmann, and N. Fournier. Exploring the impact of thermally controlled crustal viscosity on volcanic ground deformation. *Journal of Geophysical Research: Solid Earth*, 126(8):e2020JB020724, 2021.
[31] T. Heister, J. Dannberg, R. Gassmöller, and W. Bangerth. High accuracy mantle convection simulation through modern numerical methods. II: Realistic models and problems. *Geophysical Journal International*, 210(2):833–851, 2017.
[32] S. T. Henderson and M. E. Pritchard. Time-dependent deformation of Uturuncu volcano, Bolivia, constrained by GPS and InSAR measurements and implications for source models. *Geosphere*, 13(6):1834–1854, 2017.
[33] J. Hickey and J. Gottsmann. Benchmarking and developing numerical finite element models of volcanic deformation. *Journal of Volcanology and Geothermal Research*, 280:126–130, 2014.
[34] J. Hickey, J. Gottsmann, and P. Mothes. Estimating volcanic deformation source parameters with a finite element inversion: The 2001–2002 unrest at cotopaxi volcano, ecuador. *Journal of Geophysical Research: Solid Earth*, 120(3):1473–1486, 2015.
[35] C. Huber, M. Townsend, W. Degruyter, and O. Bachmann. Optimal depth of subvolcanic magma chamber growth controlled by volatiles and crust rheology. *Nature Geoscience*, 12(9):762–768, 2019.
[36] A. M. Jellinek and D. J. DePaolo. A model for the origin of large silicic magma chambers: precursors of caldera-forming eruptions. *Bulletin of Volcanology*, 65(5):363–381, 2003.
[37] O. Karakas, W. Degruyter, O. Bachmann, and J. Dufek. Lifetime and size of shallow magma bodies controlled by crustal-scale magmatism. *Nature Geoscience*, 10(6):446–450, 2017.
[38] L. Karlstrom, J. Dufek, and M. Manga. Magma chamber stability in arc and continental crust. *Journal of Volcanology and Geothermal Research*, 190(3):249–270, 2010.
[39] L. Karlstrom, S. R. Paterson, and A. M. Jellinek. A reverse energy cascade for crustal magma transport. *Nature Geoscience*, 10(8):604–608, 2017.
[40] S. Larsson and V. Thomée. *Partial differential equations with numerical methods*, volume 45. Springer Science & Business Media, 2008.
[41] H. C. Lau and B. K. Holtzman. "Measures of dissipation in viscoelastic media" extended: Toward continuous characterization across very broad geophysical time scales. *Geophysical Research Letters*, 46(16):9544–9553, 2019.
[42] H. C. Lau, B. K. Holtzman, and C. Havlin. Toward a self-consistent characterization of lithospheric plates using full-spectrum viscoelasticity. *AGU Advances*, 1(4):e2020AV000205, 2020.
[43] H. Le Mével, P. Gregg, and K. Feigl. Magma injection into a long-lived reservoir to explain geodetically measured uplift: Application to the 2007-2014 unrest episode at Laguna del Maule volcanic field, Chile. *Journal of Geophysical Research: Solid Earth*, 121:6092–6108, 2016.
[44] Y. Liao, S. A. Soule, M. Jones, and H. Le Mével. The mechanical response of a magma chamber with poroviscoelastic crystal mush. *Journal of Geophysical Research: Solid Earth*, 126(4):e2020JB019395, 2021.
[45] T. Masterlark, M. Haney, H. Dickinson, T. Fournier, and C. Searcy. Rheologic and structural controls on the deformation of okmok volcano, alaska: Fems, insar, and ambient noise tomography. *Journal of Geophysical Research: Solid Earth*, 115:1–22, 2010.
[46] D. F. McTigue. Elastic stress and deformation near a finite spherical magma body: resolution of the point source paradox. *Journal of Geophysical Research: Solid Earth*, 92(B12):12931–12940, 1987.
[47] T. Mittal and M. A. Richards. Volatile degassing from magma chambers as a control on volcanic eruptions. *Journal of Geophysical Research Solid Earth*, 124(9):7869–7901, 2019.
[48] K. Mogi. Relations between the eruptions of various volcanoes and the deformations of the ground surfaces around them. *Bulletin of the Earthquake Research Institute*, 36:99–134, 1958.
[49] A. M. Morales Rivera, F. Amelung, F. Albino, and P. M. Gregg. Impact of crustal rheology on temperature-dependent viscoelastic models of volcano deformation: Application to Taal Volcano, Philippines. *Journal of Geophysical Research: Solid Earth*, 115:978–994, 2019.
[50] L. Moresi, F. Dufour, and H.-B. Mühlhaus. Mantle convection modeling with viscoelastic/brittle lithosphere: Numerical methodology and plate tectonic modeling. *Pure and applied Geophysics*, 159(10):2335–2356, 2002.
[51] R. Muki and E. Sternberg. On Transient Thermal Stresses in Viscoelastic Materials With Temperature-Dependent Properties. *Journal of Applied Mechanics*, 28(2):193–207, 06 1961.
[52] B. Mullet and P. Segall. The surface deformation signature of a transcrustal, crystal mush-dominant magma system. *Journal of Geophysical Research: Solid Earth*, 127(5):e2022JB024178, 2022.

[53] A. Newman, T. H. Dixon, G. Ofoegbu, and J. E. Dixon. Geodetic and seismic constraints on recent activity at long valley caldera, california: evidence for viscoelastic rheology. *Journal of Volcanology and Geothermal Research*, 105(3):183–206, 2001.

[54] C. Novoa, D. Remy, M. Gerbault, J. Baez, A. Tassara, L. Cordova, C. Cardona, M. Granger, S. Bonvalot, and F. Delgado. Viscoelastic relaxation: A mechanism to explain the decennial large surface displacements at the Laguna del Maule silicic volcanic complex. *Earth and Planetary Science Letters*, 521:46–59, 2019.

[55] R. O'connell and B. Budiansky. Measures of dissipation in viscoelastic media. *Geophysical Research Letters*, 5(1):5–8, 1978.

[56] E. Rivalta, F. Corbi, L. Passarelli, V. Acocella, T. Davis, and M. A. Di Vito. Stress inversions to forecast magma pathways and eruptive vent location. *Science advances*, 5(7):eaau9784, 2019.

[57] P. J. Roache. *Verification and validation in computational science and engineering*, volume 895. Hermosa Albuquerque, NM, 1998.

[58] M. Schetzen. *Linear Time-Invariant Systems.* The Institute of Electrical and Electronics Engineers, 1 edition, 2003.

[59] J. Schöberl. NETGEN an advancing front 2D/3D-mesh generator based on abstract rules. *Computing and Visualization in Science*, 1(1):41–52, 1997.

[60] J. Schöberl. NGSolve. `http://ngsolve.org`, 2010–2022.

[61] P. Segall. *Earthquake and volcano deformation.* Princeton University Press, 2010.

[62] P. Segall. Repressurization following eruption from a magma chamber with a viscoelastic aureole. *Journal of Geophysical Research: Solid Earth*, 121(12):8501–8522, 2016.

[63] P. Segall. Magma chambers: what we can, and cannot, learn from volcano geodesy. *Philosophical Transactions of the Royal Society A*, 377(2139), 2019.

[64] F. Sigmundsson, V. Pinel, B. Lund, F. Albino, C. Pagli, H. Geirsson, and E. Sturkell. Climate effects on volcanism: influence on magmatic systems of loading and unloading from ice mass variations, with examples from Iceland. *Philosophical Transactions of the Royal Society A*, 368(1919), 2010.

[65] R. S. J. Sparks, K. Cashman, and E. Calais. Dynamic magma systems: Implications for forecasting volcanic activity. *Elements*, 13(1):35–40, 2017.

[66] M. Townsend. Linking surface deformation to thermal and mechanical magma chamber processes. *Earth and Planetary Science Letters*, 577:117–272, 2022.

[67] M. Townsend, C. Huber, W. Degruyter, and O. Bachmann. Magma chamber growth during intercaldera periods: Insights from thermo-mechanical modeling with applications to Laguna del Maule, Campi Flegrei, Santorini, and Aso. *Geochemistry, Geophysics, Geosystems*, 20(3):1574–1591, 2019.

[68] D. Walwer, M. Ghil, and E. Calais. Oscillatory nature of the Okmok volcano's deformation. *Philosophical Transactions of the Royal Society A*, 506:76–86, 2021.

[69] T. Yamasaki, T. Kobayashi, T. Wright, and Y. Fukahata. Viscoelastic crustal deformation by magmatic intrusion: A case study in the Kutcharo caldera, eastern Hokkaido, Japan. *Journal of Volcanology and Geothermal Research*, 349:128–145, 2018.

[70] Y. Zhan and P. Gregg. How accurately can we model magma reservoir failure with uncertainties in host rock rheology? *Journal of Geophysical Research: Solid Earth*, 124(8):8030–8042, 2019.

[71] X. Zhong, M. Dabrowski, and B. Jamtveit. Analytical solution for the stress field in elastic half-space with a spherical pressurized cavity or inclusion containing eigenstrain. *Geophysical Journal International*, 216(2):1100–1115, 2019.

Department of Computer and Information Science, University of Oregon, Eugene, OR, USA

Department of Computer and Information Science, University of Oregon, Eugene, OR, USA

Department of Earth Sciences, University of Oregon, Eugene, OR, USA

Department of Mathematics and Statistics, Portland State University, Portland, OR, USA

Department of Mathematics and Statistics, Portland State University, Portland, OR, USA